

## Compressibility effect in hypersonic boundary layer with isothermal wall condition

Dehao Xu<sup>1</sup>,<sup>✉</sup> Jianchun Wang<sup>2,\*</sup>, Minping Wan,<sup>2</sup> Changping Yu,<sup>3</sup>  
Xinliang Li,<sup>3</sup> and Shiyi Chen<sup>1,2,†</sup>

<sup>1</sup>*State Key Laboratory of Turbulence and Complex Systems, College of Engineering, Peking University, Beijing 100871, People's Republic of China*

<sup>2</sup>*Guangdong Provincial Key Laboratory of Fundamental Turbulence Research and Applications, Center for Complex Flows and Soft Matter Research, Department of Mechanics and Aerospace Engineering, Southern University of Science and Technology, Shenzhen 518055, People's Republic of China*

<sup>3</sup>*Laboratory of High Temperature Gas Dynamics, Institute of Mechanics, Chinese Academy of Sciences, Beijing 100190, People's Republic of China*



(Received 1 September 2020; accepted 10 May 2021; published 24 May 2021)

The compressibility effect in isothermal hypersonic boundary layer is studied with direct numerical simulation (DNS) using Helmholtz decomposition. The dilatational components of the diagonal Reynolds stress are enhanced by the cold wall condition in the near-wall region. The outward (Q1) and ejection (Q2) events are mainly located in the expansion region, while the inward (Q3) and sweep (Q4) events are primarily situated in the compression region near the wall. It is found that the cold wall condition can enhance the inward (Q3) event mainly in the compression region and enhance the ejection (Q2) event mainly in the expansion region near the wall. In particular, the cold wall can significantly enhance the positive streamwise solenoidal fluctuating velocity and negative wall-normal dilatational fluctuating velocity events. Moreover, the cold wall condition enhances the positive correlation of streamwise velocity fluctuation and fluctuating temperature, and suppresses the negative correlation of wall-normal velocity fluctuation and fluctuating temperature in the near-wall region, while it slightly weakens the negative correlation of streamwise velocity fluctuation and fluctuating temperature and the positive correlation of wall-normal velocity fluctuation and fluctuating temperature far from the wall. It is also found that the dilatational components of correlations are dominated in the near-wall region, while the solenoidal components govern the correlations far from the wall. Most of the interactions among mean and fluctuating fields of kinetic and internal energy are governed by the solenoidal components, except for the terms associated with the pressure, which are governed by the dilatational components.

DOI: [10.1103/PhysRevFluids.6.054609](https://doi.org/10.1103/PhysRevFluids.6.054609)

### I. INTRODUCTION

The properties and mechanisms of supersonic and hypersonic turbulent boundary layers attract significant attention for their extraordinary importance in the aerospace industry [1–3]. Due to the prominent influence of compressibility, supersonic and hypersonic turbulent boundary layers are more complicated than the incompressible turbulent boundary layer [4–31]. The compressibility effect due to the existence of the eddy shocklets embedded in turbulence is remarkably significant

\*wangjc@sustech.edu.cn

†chensy@sustech.edu.cn

in supersonic and hypersonic turbulent boundary layers, and its influence should be carefully investigated.

A significant difference between supersonic and hypersonic turbulent boundary layers is the wall temperature condition. If the aircraft flies at the supersonic speed, the wall temperature is essentially considered as adiabatic, while for the aircraft at hypersonic speed, the wall temperature is remarkably lower than the adiabatic wall temperature, which is mainly caused by the considerable radiative cooling and internal heat transfer. The mechanism of the adiabatic supersonic boundary layer has been investigated by other researchers [7–9, 15–19, 25]. However, due to the inherently large computational cost and occurrence of strong shock waves, the structures and statistics of the isothermal hypersonic boundary layer are rarely investigated, which is very important in the design of supersonic aircrafts. Only a small number of works have paid attention to the properties of the isothermal hypersonic boundary layer [4, 6, 22, 24]. Duan *et al.* [4] carried out direct numerical simulation (DNS) of the isothermal hypersonic turbulent boundary layer at Mach number 5, with the ratio of the wall-to-edge temperature  $T_w/T_\delta$  ranging from 1.0 to 5.4. They found that many of the scaling relations used to describe adiabatic compressible boundary layer statistics, including Morkovin’s scaling, Walz’s equation, and the strong Reynolds analogy (SRA), are also satisfied in nonadiabatic cases. They showed that compressibility effect is enhanced by wall cooling but remains insignificant. Chu *et al.* [24] performed DNS of hypersonic turbulent boundary layer at Mach number 4.9 with the ratio of wall temperature to recovery temperature from 0.5 to 1.5. They studied many fundamental properties relevant to the influence of wall temperature on Morkovin’s scaling, the SRA, and coherent vortical structures. They found that the cold wall temperature has negligible influence on these scaling relations. Liang and Li [22] performed DNS of hypersonic turbulent boundary layer at Mach number 8 with an extreme cold wall condition. They assessed the wall temperature effect on the mean velocity profile, Walz’s equation, the SRA, and turbulent energy budget. They found that the high Mach number with cold wall induces strong compressibility effect. Zhang *et al.* [6] presented a direct numerical simulation database of spatially evolving turbulent boundary layers with Mach number ranging from 2.5 to 14 and wall-to-recovery temperature from 0.18 to 1.0. They inspected the Morkovin’s scaling, SRA, and thermodynamic fluctuations as well as the Reynolds stress budget.

Previous investigations on hypersonic turbulent boundary layer with isothermal boundary condition [4, 6, 22, 24] were focused on statistical relation of flow fields, including the van Driest transformation for mean velocity, Walz’s relation, Morkovin’s scaling, and the strong Reynolds analogy (SRA), which are proved to be valid when the free-stream Mach number  $M \approx 5$  and partly valid for  $M = 8$ . It is crucial to further investigate the influence of the isothermal wall condition on the genuine compressibility effect in the hypersonic boundary layer.

Helmholtz decomposition of the velocity field is a straightforward way to explore the compressibility effect of flow fields. Helmholtz decomposition has been used in the analysis of compressible isotropic turbulence [32–40], homogenous shear flows [41–44], and turbulent channel flows [45]. Helmholtz decomposition has also been applied in the supersonic turbulent boundary layer [16], where the dilatational component has been ignored. In this paper, Helmholtz decomposition is introduced to evaluate the compressibility effect in the isothermal hypersonic turbulent boundary layer.

The rest of the paper is organized as follows. The governing equations and numerical methodology are described in Sec. II. Flow statistics are demonstrated in Sec. III. Properties of turbulent shear stress are studied in Sec. IV. Correlations between velocity fluctuations and fluctuating temperature are presented in Sec. V. The kinetic and internal energy budgets are illustrated in Sec. VI. Finally, summary and conclusion are made in Sec. VII.

## II. GOVERNING EQUATIONS AND NUMERICAL METHODOLOGY

A set of reference scales are introduced to normalize the variables in the hypersonic turbulent boundary layer [22, 32–34, 38]. The reference density  $\rho_\infty$ , viscosity  $\mu_\infty$ , thermal conductivity  $\kappa_\infty$ ,

length  $L_\infty$ , freestream velocity  $U_\infty$ , pressure  $p_\infty = \rho_\infty U_\infty^2$ , freestream temperature  $T_\infty$ , and energy per unit volume  $\rho_\infty U_\infty^2$  are utilized. Thus, there are three nondimensional governing parameters: the Reynolds number  $Re = \rho_\infty U_\infty L_\infty / \mu_\infty$ , the Mach number  $M = U_\infty / c_\infty$ , and the Prandtl number  $Pr = \mu_\infty C_p / \kappa_\infty$ . The parameter  $\alpha$  is defined as  $\alpha = Pr Re (\gamma - 1) M^2$ , where  $Pr$  is assumed to be equal to 0.7.  $\gamma = C_p / C_v$  is the ratio of specific heat at constant pressure  $C_p$  to that at constant volume  $C_v$ , which is assumed to be equal to 1.4.

The following dimensionless Navier-Stokes equations in conservation form are solved numerically [32–34,38]:

$$\frac{\partial \rho}{\partial t} + \frac{\partial (\rho u_j)}{\partial x_j} = 0, \quad (1)$$

$$\frac{\partial (\rho u_i)}{\partial t} + \frac{\partial [\rho u_i u_j + p \delta_{ij}]}{\partial x_j} = \frac{1}{Re} \frac{\partial \sigma_{ij}}{\partial x_j}, \quad (2)$$

$$\frac{\partial E}{\partial t} + \frac{\partial [(E + p)u_j]}{\partial x_j} = \frac{1}{\alpha} \frac{\partial}{\partial x_j} \left( \kappa \frac{\partial T}{\partial x_j} \right) + \frac{1}{Re} \frac{\partial (\sigma_{ij} u_i)}{\partial x_j}, \quad (3)$$

$$p = \rho T / (\gamma M^2), \quad (4)$$

where  $\rho$  is the density,  $p$  is the pressure,  $u_i$  is the velocity component, and  $T$  is the temperature. The viscous stress  $\sigma_{ij}$  is defined as

$$\sigma_{ij} = \mu \left( \frac{\partial u_i}{\partial x_j} + \frac{\partial u_j}{\partial x_i} \right) - \frac{2}{3} \mu \theta \delta_{ij}, \quad (5)$$

where  $\theta = \frac{\partial u_k}{\partial x_k}$  is the velocity divergence. The total energy per unit volume  $E$  is

$$E = \frac{p}{\gamma - 1} + \frac{1}{2} \rho (u_j u_j). \quad (6)$$

The convection terms are approximated by the seventh-order weighted essentially nonoscillatory scheme [46], and the viscous terms are discretized by the eighth-order central difference scheme. The third-TVD type Runge-Kutta method is utilized for time advancing [22].

In this study,  $\bar{f}$  represents the Reynolds average (spanwise and time average) of  $f$ , and the fluctuating counterpart of the Reynolds average is defined as  $f' = f - \bar{f}$ . Moreover,  $\tilde{f} = \frac{\rho \bar{f}}{\bar{\rho}}$  denotes the Favre average of  $f$ . The fluctuating counterpart is  $f'' = f - \tilde{f}$ .

The DNS is carried out using the OPENCFD code developed by Li *et al.*, which has been widely used and validated in compressible transitional and turbulent wall-bounded flows [22,23,31,47]). The spatially evolving turbulent boundary layer is simulated with the following boundary conditions: the inflow and outflow boundary conditions, a wall boundary condition, an upper far-field boundary condition, and a periodic boundary condition in the spanwise direction. To be specific, a time-independent laminar compressible boundary-layer similarity solution is imposed at the inflow boundary. A region of wall blowing and suction is implemented at  $4.5 \leq x \leq 5$  to induce the laminar-to-turbulent transition. The blowing and suction disturbance is applied on the wall-normal velocity component on the wall, and the specific form is expressed as follows [15,48,49]:

$$v(x, z, t)|_{\text{wall}} = AU_\infty f(x)g(z)h(t), \quad x_a \leq x \leq x_b. \quad (7)$$

Here  $A$  is the amplitude of the disturbance and  $A = 0.04$  and  $0.08$  in M8T1 and M8T2, respectively.  $U_\infty$  is the freestream streamwise velocity.  $x_a = 4.5$  and  $x_b = 5.0$  are the beginning and the end of the blowing and suction zone, respectively. Moreover,

$$f(x) = 4 \sin \theta (1 - \cos \theta) / \sqrt{27}, \quad \theta = 2\pi (x - x_a) / (x_b - x_a), \quad (8)$$

TABLE I. Summary of computational parameters for the DNS study. The computational domains  $L_x$ ,  $L_y$ , and  $L_z$  are nondimensionalized by 1 inch [15].

Case	$M_\infty$	$\text{Re}_\infty$	$T_w/T_\infty$	$T_w/T_r$	$L_x \times L_y \times L_z$
M8T1	8	$2 \times 10^6$	1.9	0.15	$19 \times 0.7 \times 0.35$
M8T2	8	$5 \times 10^6$	10.03	0.80	$41 \times 0.7 \times 0.6$
Case	$N_x \times N_y \times N_z$	$\Delta x^+$	$\Delta y_w^+$	$\Delta z^+$	
M8T1	$9000 \times 200 \times 1280$	11.2	0.5	4.5	
M8T2	$12\,500 \times 200 \times 640$	12.2	0.5	4.6	

$$g(z) = \sum_{l=1}^{l_{\max}} Z_l \sin [2\pi l(z/L_z + \phi_l)], \quad \sum_{l=1}^{l_{\max}} Z_l = 1, \quad Z_l = 1.25Z_{l+1}, \quad (9)$$

$$h(t) = \sum_{m=1}^{m_{\max}} T_m \sin [2\pi m(\beta t + \phi_m)], \quad \sum_{m=1}^{m_{\max}} T_m = 1, \quad T_m = 1.25T_{m+1}. \quad (10)$$

Here  $L_z$  is the size of the spanwise domain, and  $l_{\max} = 10$ ,  $m_{\max} = 5$ , and  $\beta = 1.57$  and  $0.5$ , respectively.  $\phi_l$  and  $\phi_m$  are the phase difference and taken as random numbers ranging between 0 and 1.

For the outflow boundary condition, all the flow fields are extrapolated from the interior points to the outflow boundary points except the pressure in the subsonic region of the boundary layer. The pressure in the subsonic region is set equal to the value of the first grid point where the flow is supersonic. In order to inhibit the reflection of disturbance due to the numerical treatment of the outflow boundary condition, a progressively coarse grid is implemented in the streamwise direction near the outflow boundary condition [15]. Moreover, the nonslip condition is applied for the wall boundary, and the nonreflecting boundary condition is imposed for the upper boundary [15]. Further descriptions of the boundary conditions can be found in Refs. [15,22].

A cold wall case and a less cold wall case, which are denoted as M8T1 and M8T2, respectively, are calculated and analyzed in the present study. The fundamental parameters of the database are listed in Table I. Here  $M_\infty = U_\infty/c_\infty$  and  $\text{Re}_\infty = \rho_\infty U_\infty L_\infty / \mu_\infty$  are the freestream Mach number and Reynolds number, respectively.  $T_w$  is the wall temperature.  $T_\infty$  is the freestream temperature, which is assumed to be  $T_\infty = 169.44$  K. The wall temperatures in M8T1 and M8T2 are  $T_w/T_\infty = 1.9$  and  $10.03$ , respectively. The recovery temperature  $T_r$  is defined as  $T_r = T_\infty \{1 + r[(\gamma - 1)/2]M_\infty^2\}$  with recovery factor  $r = 0.9$  [4]. The computational domains  $L_x$ ,  $L_y$ , and  $L_z$  are nondimensionalized by  $L_\infty = 1$  inch [15].  $x$ ,  $y$ , and  $z$  are the streamwise, wall-normal, and spanwise directions, respectively.  $\delta_v = \overline{\mu_w} / (\overline{\rho_w} u_\tau)$  is the viscous length scale.  $u_\tau = \sqrt{\tau_w / \rho_w}$  is the friction velocity, and  $\tau_w = (\mu \frac{\partial \overline{U}}{\partial y})_{y=0}$  is the wall shear stress.  $\Delta x^+ = \Delta x / \delta_v$  is the normalized spacing of streamwise direction.  $\Delta y_w^+ = \Delta y_w / \delta_v$  is the normalized spacing of the first point off the wall.  $\Delta z^+ = \Delta z / \delta_v$  is the normalized spacing of the spanwise direction.  $\rho_w$  is the density on the wall.  $\overline{\mu_w}$  and  $\overline{\rho_w}$  are the Reynolds average of the viscosity and density on the wall, respectively. Validation of the accuracy of the current numerical simulations is shown in the Appendix.

Data in a small streamwise window of  $[x_a - 0.5\delta, x_a + 0.5\delta]$  extracted from the fully developed region of the DNS are used for the following analysis. Here  $x_a = 14$  and  $30$  for M8T1 and M8T2, respectively,  $\delta = 0.13$  and  $0.28$  for M8T1 and M8T2, respectively. The flow statistics analyzed in the following sections are calculated in the streamwise window of  $[x_a - 0.5\delta, x_a + 0.5\delta]$ . It is noted that the size of the streamwise window is similar with Ref. [6]. One hundred flow-field snapshots



TABLE II. Global flow properties determined by the fully developed region of hypersonic boundary layer.

Case	$Re_\infty$	$Re_\tau$	$Re_\theta$	$Re_{\delta_2}$
M8T1	$2 \times 10^6$	2444	$1.02 \times 10^4$	6018
M8T2	$5 \times 10^6$	1386	$3.22 \times 10^4$	6563

spanning a time interval of approximately  $44\delta/U_\infty$  for M8T1 and  $20\delta/U_\infty$  for M8T2 are used for analysis.

On basis of Helmholtz decomposition, the velocity field ( $\mathbf{u}$ ) can be decomposed into a solenoidal ( $\mathbf{u}_s$ ) and a dilatational ( $\mathbf{u}_d$ ) component ( $\mathbf{u} = \mathbf{u}_s + \mathbf{u}_d$ ), which satisfies  $\nabla \cdot \mathbf{u}_s = 0$  and  $\nabla \times \mathbf{u}_d = 0$ , respectively. The two components can be obtained from the velocity field  $\mathbf{u}$  by solving Poisson equations of the vector potential  $\mathbf{A}$  and scalar potential  $\varphi$ ,

$$\nabla^2 \mathbf{A} = -\nabla \times \mathbf{u}, \quad \nabla^2 \varphi = \nabla \cdot \mathbf{u}. \quad (11)$$

Accordingly, the solenoidal and dilatational components can be obtained by

$$\mathbf{u}_s = \nabla \times \mathbf{A}, \quad \mathbf{u}_d = \nabla \varphi. \quad (12)$$

With the wall boundary conditions given by Ref. [50],

$$\frac{\partial \varphi}{\partial y} = 0, \quad \frac{\partial A_y}{\partial y} = 0, \quad A_x = A_z = 0, \quad (13)$$

the vector potential  $\mathbf{A}$  is unique [16,45,50]. A mirror symmetry is applied on the data in a pretty large streamwise window of  $[x_a - 4\delta, x_a + 4\delta]$  to generate an artificial periodic condition in streamwise direction. It is noted that the artificial periodic condition barely has any influence on the flow statistics of the data in a small streamwise window of  $[x_a - 0.5\delta, x_a + 0.5\delta]$ . If the streamwise window is further increased to  $[x_a - 8\delta, x_a + 8\delta]$ , the flow statistics of the data in  $[x_a - 0.5\delta, x_a + 0.5\delta]$  is unchanged. Then the Poisson equations (11) are discretized spectrally in the streamwise ( $x$ ) and spanwise ( $z$ ) directions, and by sixth-order central difference in the wall-normal ( $y$ ) direction.

The velocity field can be divided into  $\mathbf{u} = \tilde{\mathbf{U}} + \mathbf{u}''$ , where  $\tilde{\mathbf{U}}$  is the Favre average of velocity field and  $\mathbf{u}''$  is the fluctuating counterpart. Moreover, the fluctuating counterpart can be decomposed into a solenoidal ( $\mathbf{u}_s''$ ) and a dilatational ( $\mathbf{u}_d''$ ) component.

Several relevant Reynolds numbers are important in the compressible boundary layer. The friction Reynolds number  $Re_\tau = \overline{\rho_w} u_\tau \delta / \overline{\mu_w}$  is defined as the ratio of the boundary layer thickness and the viscous length scale. The Reynolds number based on the momentum thickness  $\theta$  and the wall viscosity,  $Re_\theta = \rho_\infty u_\infty \theta / \overline{\mu_w}$ , is defined as the ratio of the highest momentum to the wall shear stress. Here the momentum thickness  $\theta$  is defined as

$$\theta = \int_0^\delta \frac{\overline{\rho U}}{\rho_\infty U_\infty} \left(1 - \frac{\overline{U}}{U_\infty}\right) dy, \quad (14)$$

where  $\overline{\rho}$  and  $\overline{U}$  are the Reynolds average of density  $\rho$  and streamwise velocity  $u$ , respectively.  $\rho_\infty$  and  $U_\infty$  are the freestream density and streamwise velocity, respectively.  $\delta$  is the boundary layer thickness.  $Re_\theta = \rho_\infty u_\infty \theta / \mu_\infty$  is the Reynolds number based on the momentum thickness  $\theta$ . The above global flow properties calculated from the fully developed region of the DNS are listed in Table II.

### III. FLOW STATISTICS

The van Driest transformed velocity,  $U_{VD}^+$ , is defined as [51]

$$U_{VD}^+ = \int_0^{U^+} (\overline{\rho} / \overline{\rho_w})^{1/2} dU^+, \quad (15)$$

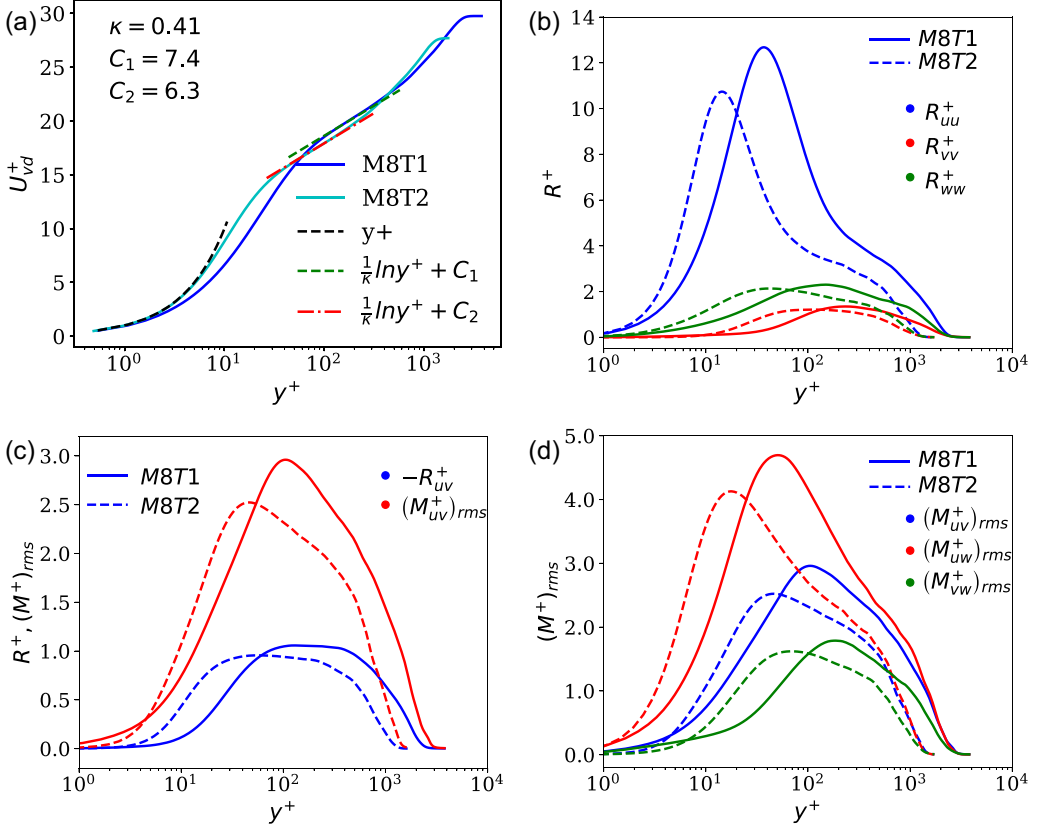


FIG. 1. (a) The van Driest transformed velocity. (b) The diagonal components of the normalized Reynolds stress  $R_{uu}^+$ ,  $R_{vv}^+$ , and  $R_{ww}^+$  along the wall-normal direction. (c) The turbulent shear stress  $-R_{uv}^+$  and the r.m.s. value of the normalized tensor  $(M_{uv}^+)_{rms}$  along the wall-normal direction. (d) The r.m.s. values of the off-diagonal components of the normalized tensor  $(M_{uv}^+)_{rms}$ ,  $(M_{uw}^+)_{rms}$ , and  $(M_{vw}^+)_{rms}$  along the wall-normal direction.

where  $\bar{\rho}$  is the Reynolds average of density and  $\bar{\rho}_w$  is the Reynolds average of density on the wall.  $U^+$  is defined as  $U^+ = \bar{U}/u_\tau$ . The van Driest transformed velocity  $U_{VD}^+$  is plotted in Fig. 1(a). It is found that  $U_{VD}^+$  satisfies the law of wall  $U^+ = y^+$  in both M8T1 and M8T2, while the range of the law of the wall is smaller in M8T1 mainly due to the cold wall condition. Moreover, the log law  $U_{VD}^+ = \frac{1}{\kappa} \ln y^+ + C$  is also satisfied in M8T1 and M8T2, where  $\kappa \approx 0.41$  is similar to the incompressible values [11], while the additive constant  $C$  is slightly larger than that in incompressible boundary layer. The additive constant  $C$  in M8T1 is larger than that in M8T2, which is consistent with the observation found in Ref. [24].

The normalized tensor  $M_{ij}^+$  is defined as  $M_{ij}^+ = \frac{\rho u_i' u_j'}{\tau_w}$ . The average of the normalized tensor  $M_{ij}^+$ , i.e., the normalized Reynolds stress, is denoted as  $R_{ij}^+ = \frac{\langle \rho \widetilde{u_i' u_j'} \rangle}{\tau_w}$ , and the r.m.s. value of the normalized tensor  $M_{ij}^+$  is defined as  $(M_{ij}^+)_{rms} = \sqrt{\langle (M_{ij}^+ - R_{ij}^+)^2 \rangle}$ . The diagonal components of the normalized Reynolds stress  $R_{uu}^+$ ,  $R_{vv}^+$ , and  $R_{ww}^+$  along wall-normal direction are plotted in Fig. 1(b). It is found that the peak of  $R_{uu}^+$  is much larger than the peaks of  $R_{vv}^+$  and  $R_{ww}^+$ , indicating a strong intensity of the streamwise velocity fluctuation. Moreover, it is demonstrated that the peak of  $R_{uu}^+$  in M8T1 is significantly larger than that in M8T2, while the peaks of  $R_{vv}^+$  and  $R_{ww}^+$  in M8T1 are slightly smaller than those in M8T2, indicating that the peak of streamwise

velocity fluctuation increases with strong compressibility, while the peaks of wall-normal and spanwise velocity fluctuations slightly decrease with strong compressibility, which is consistent with observations made in Refs. [5,6,14,45]. The decrease of wall-normal and spanwise velocity fluctuations and the increase of streamwise velocity fluctuation with the cold wall give rise to the reduced mixing in the wall-normal and spanwise directions. Consequently, the energy transfer by eddies along spanwise direction are decreased, leading to more coherent structures with the cold wall. The turbulent shear stress  $-R_{uv}^+$  and the r.m.s. value of the normalized tensor  $(M_{uv}^+)_{\text{rms}}$  along the wall-normal direction are plotted in Fig. 1(c). It is found that  $(M_{uv}^+)_{\text{rms}}$  is much larger than  $-R_{uv}^+$ , indicating the cancellation of strong negative and weak positive values of the normalized tensor  $M_{uv}^+$ . The other two off-diagonal components of the normalized Reynolds stress  $R_{uv}^+$  and  $R_{vw}^+$  are zero due to homogeneity of spanwise velocity (not reported here). The r.m.s. values of the off-diagonal components of the normalized tensor  $(M_{uv}^+)_{\text{rms}}$ ,  $(M_{uv}^+)_{\text{rms}}$ , and  $(M_{uv}^+)_{\text{rms}}$  along the wall-normal direction are shown in Fig. 1(d). It is found that  $M_{uv}^+$  has the strongest fluctuating intensity and  $M_{vw}^+$  has the weakest fluctuating intensity. The peak of  $(M_{uv}^+)_{\text{rms}}$  is closest to the wall, and that of  $(M_{vw}^+)_{\text{rms}}$  is farthest from the wall.

The normalized vorticity fluctuation is defined as  $\omega_i''^+ = \omega_i'' / (u_\tau / \delta_v)$ , and the normalized dilatation fluctuation is expressed as  $\theta''^+ = \theta'' / (u_\tau / \delta_v)$ . Distributions of the normalized vorticity fluctuations  $\langle (\omega_x'')^2 \rangle^{1/2}$ ,  $\langle (\omega_y'')^2 \rangle^{1/2}$ , and  $\langle (\omega_z'')^2 \rangle^{1/2}$  along the wall-normal direction are plotted in Fig. 2(a). The streamwise and spanwise vorticity fluctuations  $\omega_x''^+$  and  $\omega_z''^+$  have the strongest intensities in the near-wall region, while the wall-normal vorticity fluctuation  $\omega_y''^+$  has the peak in the buffer layer. The intensity of the spanwise vorticity fluctuation  $\omega_z''^+$  is larger than other two components, which is similar to those found in Refs. [6,14,45]. Distribution of the normalized dilatation fluctuation  $\langle (\theta'')^2 \rangle^{1/2}$  along the wall-normal direction is plotted in Fig. 2(b). It is found that  $\langle (\theta'')^2 \rangle^{1/2}$  in M8T1 is much larger than that in M8T2, illustrating that the cold wall condition enhances the compressibility in the near-wall region. Probability density functions (PDFs) of the normalized dilatation fluctuation  $\theta''^+$  along the wall-normal direction in M8T1 and M8T2 are shown in Fig. 2(c) and 2(d), respectively. It is found that PDF of the normalized dilatation  $\theta''^+$  spans widest near the wall and becomes narrow far from the wall. Furthermore, it is shown that PDF of  $\theta''^+$  in M8T2 is nearly symmetric in the near-wall region, while negative skewness appears in the PDF of  $\theta''^+$  in M8T1, indicating that the cold wall condition enhances the compression motion in the near-wall region.

On the basis of Helmholtz decomposition, the normalized tensor  $M_{ij}^+$  can be decomposed into

$$\begin{aligned} M_{ij}^+ &= \frac{\rho u_i'' u_j''}{\tau_w} = \frac{\rho u_{s,i}'' u_{s,j}''}{\tau_w} + \frac{\rho u_{d,i}'' u_{d,j}''}{\tau_w} + \frac{\rho u_{s,i}'' u_{d,j}''}{\tau_w} + \frac{\rho u_{d,i}'' u_{s,j}''}{\tau_w} \\ &\equiv M_{is,j_s}^+ + M_{id,j_d}^+ + M_{is,j_d}^+ + M_{id,j_s}^+. \end{aligned} \quad (16)$$

Thus, the normalized Reynolds stress  $R_{ij}^+$  can be decomposed into

$$\begin{aligned} R_{ij}^+ &= \frac{\langle \rho \widetilde{u_i'' u_j''} \rangle}{\tau_w} = \frac{\langle \rho \widetilde{u_{s,i}'' u_{s,j}''} \rangle}{\tau_w} + \frac{\langle \rho \widetilde{u_{d,i}'' u_{d,j}''} \rangle}{\tau_w} + \frac{\langle \rho \widetilde{u_{s,i}'' u_{d,j}''} \rangle}{\tau_w} + \frac{\langle \rho \widetilde{u_{d,i}'' u_{s,j}''} \rangle}{\tau_w} \\ &\equiv R_{is,j_s}^+ + R_{id,j_d}^+ + R_{is,j_d}^+ + R_{id,j_s}^+. \end{aligned} \quad (17)$$

Here  $R_{is,j_s}^+$  ( $M_{is,j_s}^+$ ) and  $R_{id,j_d}^+$  ( $M_{id,j_d}^+$ ) are related to the variance of the solenoidal and dilatational velocity fields, respectively, and  $R_{is,j_d}^+$  ( $M_{is,j_d}^+$ ) and  $R_{id,j_s}^+$  ( $M_{id,j_s}^+$ ) are associated with the covariance between the solenoidal and dilatational velocity fields. The decomposed components of the diagonal Reynolds stress along the wall-normal direction are depicted in Figs. 3(a), 3(b), and 3(c). The solenoidal variance components of the diagonal Reynolds stress  $R_{uu}^+$ ,  $R_{vv}^+$ , and  $R_{ww}^+$  are dominant in the diagonal Reynolds stress  $R_{uu}^+$ ,  $R_{vv}^+$ , and  $R_{ww}^+$ . The intensities of dilatational components are much smaller than solenoidal components. It is noticed that  $R_{ud,ud}^+$ ,  $R_{vd,vd}^+$ , and  $R_{wd,wd}^+$  are much

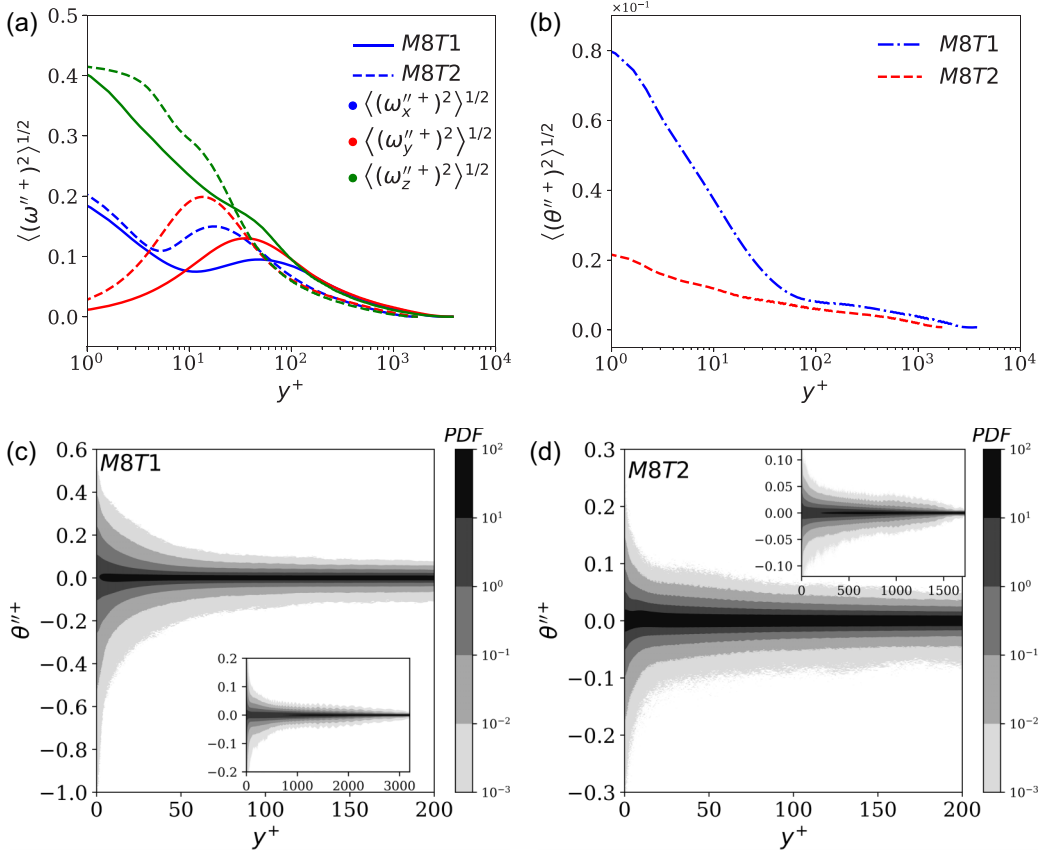


FIG. 2. (a) and (b) Distributions of (a) the normalized vorticity fluctuations  $\langle(\omega''_x)^2\rangle^{1/2}$ ,  $\langle(\omega''_y)^2\rangle^{1/2}$ , and  $\langle(\omega''_z)^2\rangle^{1/2}$  and (b) the normalized dilatation fluctuation  $\langle(\theta''^+)^2\rangle^{1/2}$  along the wall-normal direction. (c) and (d) PDF of the normalized dilatation fluctuation  $\theta''^+$  along the wall-normal direction in (c) M8T1 and (d) M8T2.

larger in M8T1 than those in M8T2, indicating that the cold wall temperature can enhance the compressibility in the near-wall region. The dilatational variance components of the streamwise and spanwise Reynolds stress  $R_{u_d u_d}^+$  and  $R_{w_d w_d}^+$  attain peaks in the near-wall region, while the wall-normal component  $R_{v_d v_d}^+$  achieves its crest in the buffer layer. It is also found that  $R_{v_d v_d}^+$  is larger than  $R_{v_s v_s}^+$  near the wall in M8T1, which is consistent with observations in Ref. [45]. This mainly accounts for the different asymptotic wall scaling, where  $v_s'' \sim y^2$  [52] due to incompressibility while  $v_d'' \sim y$  [3]. Accordingly, it is concluded that the cold wall condition enhances the compressibility in the near-wall region through increasing the streamwise and spanwise dilatational components near the wall and increasing the wall-normal dilatational component in the buffer layer. Moreover,  $u_s''$  and  $w_s''$  are negatively correlated with  $u_d''$  and  $w_d''$ , respectively, near the wall, and the negative correlation is enhanced by the cold wall. The r.m.s. values of  $2M_{u_s u_d}^+$ ,  $2M_{v_s v_d}^+$ , and  $2M_{w_s w_d}^+$  along wall-normal direction are shown in Fig. 3(d). The r.m.s. values of  $2M_{u_s u_d}^+$ ,  $2M_{v_s v_d}^+$ , and  $2M_{w_s w_d}^+$  are much larger than the average values, implying the cancellation between positive and negative values of  $2M_{u_s u_d}^+$ ,  $2M_{v_s v_d}^+$ , and  $2M_{w_s w_d}^+$ .

The decompositions of the normalized tensor  $M_{uv}^+$  and the normalized turbulent shear stress  $R_{uv}^+$  are also investigated. The average and r.m.s. values of the decomposed components of the normalized tensor  $M_{uv}^+$  are shown in Fig. 4. As expected, the solenoidal component  $R_{u_s v_s}^+$  dominates

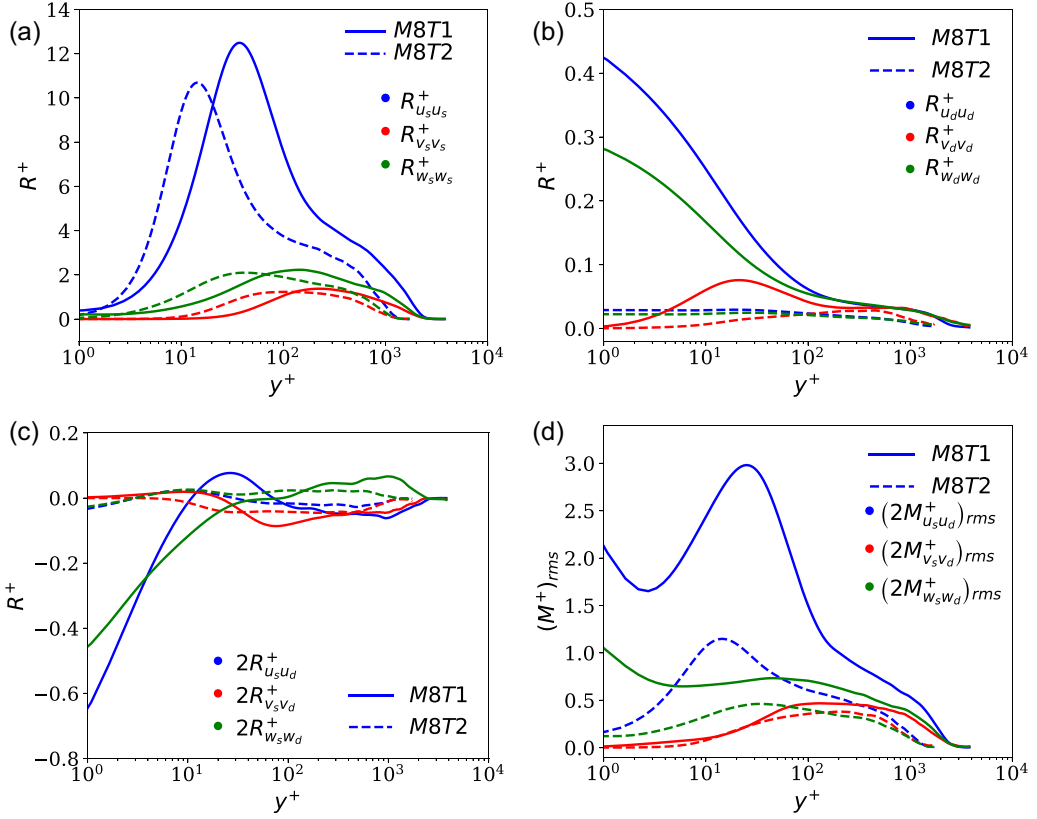


FIG. 3. (a)  $R_{u_s u_s}^+$ ,  $R_{v_s v_s}^+$ , and  $R_{w_s w_s}^+$  along wall-normal direction. (b)  $R_{u_d u_d}^+$ ,  $R_{v_d v_d}^+$ , and  $R_{w_d w_d}^+$  along the wall-normal direction. (c)  $2R_{u_s u_d}^+$ ,  $2R_{v_s v_d}^+$ , and  $2R_{w_s w_d}^+$  along the wall-normal direction. (d) The r.m.s. values of  $2M_{u_s u_d}^+$ ,  $2M_{v_s v_d}^+$ , and  $2M_{w_s w_d}^+$  along the wall-normal direction.

in the normalized turbulent shear stress  $R_{uv}^+$ . The dilatational component  $R_{u_d v_d}^+$  in M8T1 is much larger than that in M8T2 near the wall, indicating the stronger compressibility with the cold wall condition. The terms  $-R_{u_s v_s}^+$  and  $-R_{u_d v_d}^+$  are positive along the wall-normal direction, while the terms  $-R_{u_s v_d}^+$  and  $-R_{u_d v_s}^+$  are negative.  $R_{u_s v_d}^+$  is an order larger than  $R_{u_d v_s}^+$ , which is due to the largest intensity of  $u_s''$ . The above observations are consistent with those in Ref. [45]. Moreover, the cold wall enhances the correlation of  $u_s''$  and  $v_d''$ , while has negligible influence on the correlation of  $u_d''$  and  $v_s''$ . Accordingly, the increase of  $R_{u_s v_d}^+$  is mainly due to the enhancement of the intensity of  $v_d''$  caused by the stronger compressibility with the cold wall. It is also found that the r.m.s. values of  $M_{u_d v_d}^+$ ,  $M_{u_s v_d}^+$ , and  $M_{u_d v_s}^+$  are much larger than the average values, indicating strong cancellation of positive and negative values.

The instantaneous velocity fields of  $u''$ ,  $v''$ ,  $u_s''$ ,  $v_s''$ ,  $u_d''$ , and  $v_d''$  in a wall-parallel plane at  $y^+ = 10$  in M8T1 and M8T2 are shown in Figs. 5 and 6, respectively.  $u''$  exhibits the streaks, while  $v''$  has a more spotty appearance due to ejection and sweep events. It is shown that the observed streaks in M8T1 become thicker and more elongated compared with those in M8T2, indicating that the cold wall increases the streamwise coherency of near-wall streaks. Moreover, the spanwise spacing of streaks also increases with the cold wall. These observations are consistent with Ref. [4]. Furthermore, the spotty appearance due to ejection and sweep events becomes weaker in M8T1, indicating the reduced mixing in the wall-normal direction with the cold wall. These observations are consistent with above observations [shown in Fig. 1(b)] and previous findings [5,6,14,45] that

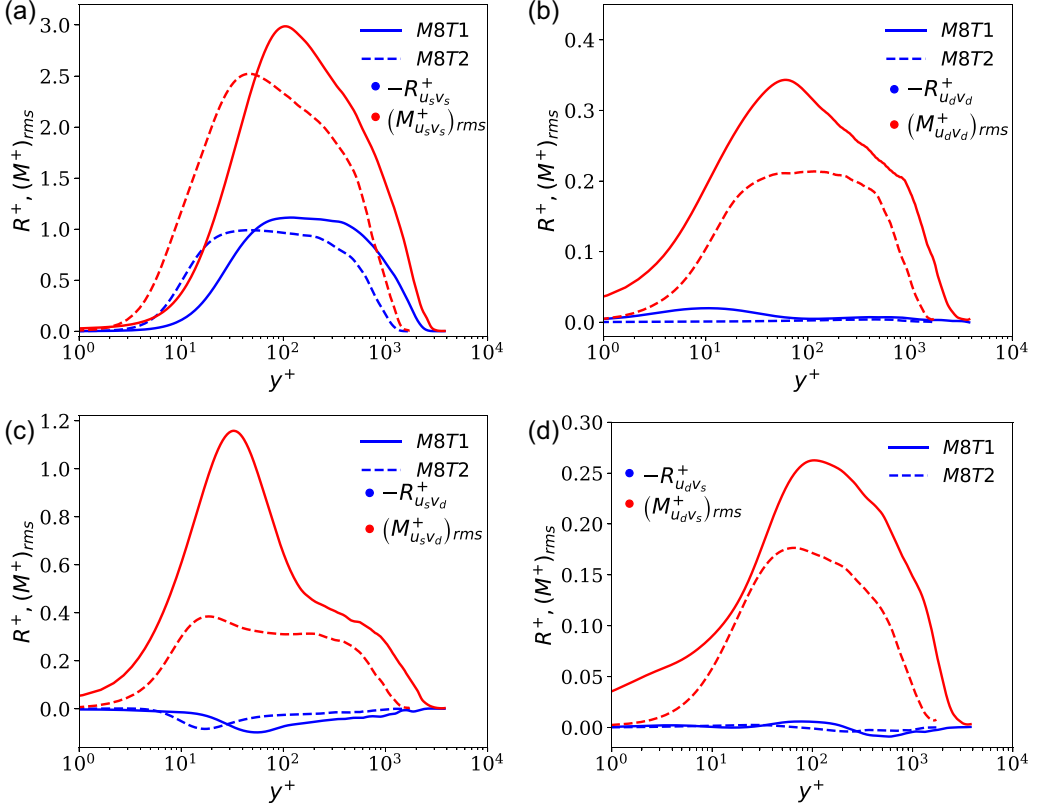


FIG. 4. The average and r.m.s. values of the decomposed components of the normalized shear second-moment fluctuating velocities tensor  $M_{uv}^+$ : (a)  $-R_{u_s v_s}^+$  and  $(M_{u_s v_s}^+)_{rms}$ , (b)  $-R_{u_d v_d}^+$  and  $(M_{u_d v_d}^+)_{rms}$ , (c)  $-R_{u_s v_d}^+$  and  $(M_{u_s v_d}^+)_{rms}$ , and (d)  $-R_{u_d v_s}^+$  and  $(M_{u_d v_s}^+)_{rms}$  along the wall-normal direction.

the wall-normal and spanwise velocity fluctuations decrease and the streamwise velocity fluctuation increases with the cold wall.  $u''_s$  and  $v''_s$  recover the streaks in  $u''$  and the spotty appearance in  $v''$ , respectively.  $u''_d$  and  $v''_d$  reveal spanwise ripples traveling like streamwise wave packets from left to right. These observations are consistent with Ref. [45]. It is also found that the intensities of  $u''_d$  and  $v''_d$  in M8T1 are much larger than those in M8T2, mainly due to the effect of the cold wall condition.

#### IV. INVESTIGATION OF THE TURBULENT SHEAR STRESS

The normalized tensor  $M_{uv}^+$  as well as the normalized turbulent shear stress  $R_{uv}^+$  should be investigated meticulously due to their direct relevance in the kinetic energy budget.

Quadrant analysis is introduced to further explore the statistical behavior of the normalized tensor  $M_{uv}^+$  as well as the normalized turbulent shear stress  $R_{uv}^+$ . On the basis of quadrant analysis, four quadrants are created by the streamwise and wall-normal velocity fluctuations, and the instantaneous turbulent shear stress located in these four quadrants are called four events [53]: (1)  $Q_1$ :  $u'' > 0$ ,  $v'' > 0$ ; (2)  $Q_2$ :  $u'' < 0$ ,  $v'' > 0$ ; (3)  $Q_3$ :  $u'' < 0$ ,  $v'' < 0$ ; and (4)  $Q_4$ :  $u'' > 0$ ,  $v'' < 0$ . The Q2 and Q4 events represent the ejection and sweep events, which are gradient-type motions and make the largest contributions to the turbulent shear stress. The Q2 event describes the motion that the near-wall low-speed streaks rise and break up under the effect of rolling vortex pairs, while the Q4 event implies the high-speed streaks in the outer layer sweep down to the near-wall fluid.



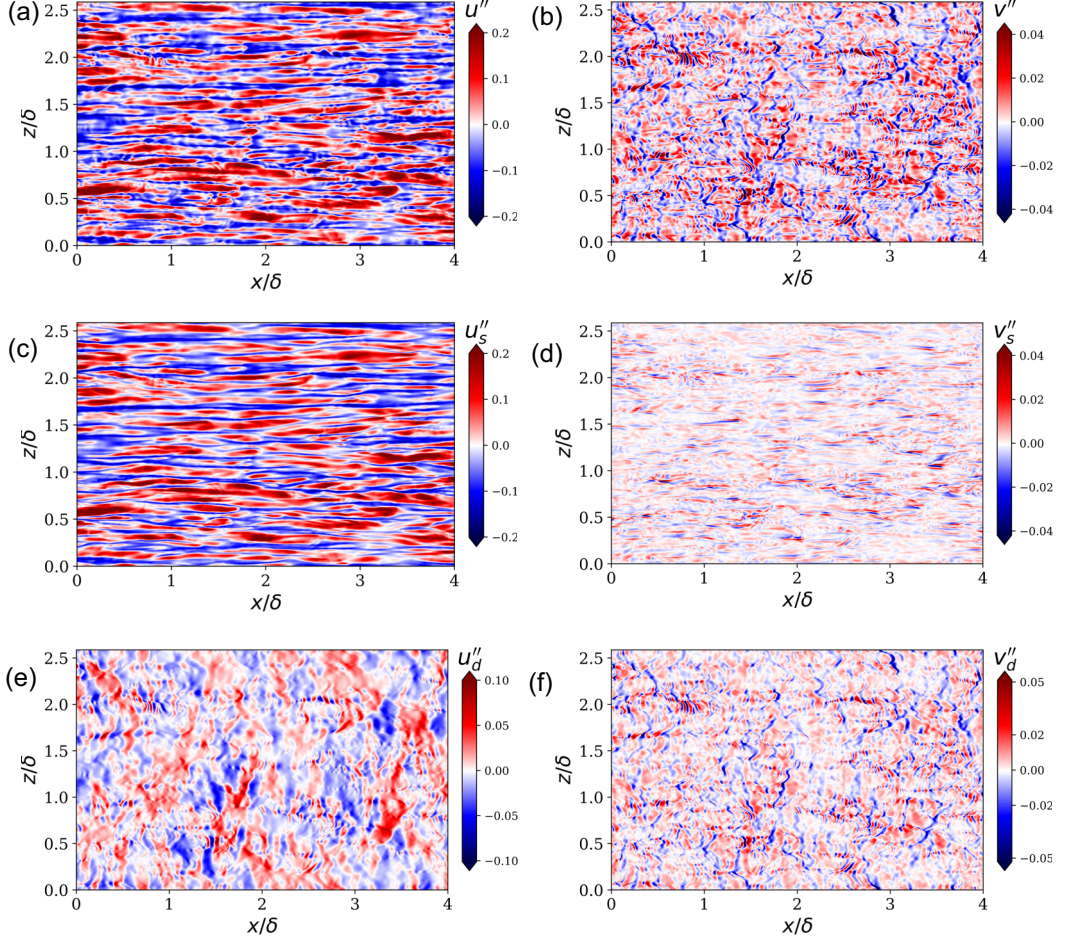


FIG. 5. Instantaneous fields of (a)  $u''$ , (b)  $v''$ , (c)  $u_s''$ , (d)  $v_s''$ , (e)  $u_d''$ , and (f)  $v_d''$  in a wall-parallel plane at  $y^+ = 10$  in M8T1.  $\delta$  is the boundary layer thickness.

The Q1 and Q3 events denote the outward and inward interactions, which are countergradient-type motions [53]. Quadrant contributions to the turbulent shear stress along the wall-normal direction in M8T1 and M8T2 are depicted in Fig. 7. It is shown that in M8T2, the Q4 (sweep) event contributes considerably more to the mean turbulent shear stress than the Q2 (ejection) event near the wall, whereas the trend reverses far from the wall. The Q1 (outward) event and Q3 (inward) event have similar contributions to the mean turbulent shear stress. These observations are consistent with incompressible wall-bounded flow [53]. However, the behaviors of these four events in M8T1 have a significant difference. The Q2 (ejection) event always contributes more to the mean turbulent shear stress than the Q4 (sweep) event, implying that the cold wall condition enhances the Q2 (ejection) event in the near-wall region. Furthermore, the magnitude of the Q3 (inward) event is larger than the Q1 (outward) event near the wall. It is also found that the magnitudes of these four events in M8T1 are larger than those in M8T2 in the near-wall region, while the magnitudes of four events in these two cases are similar far from the wall. Accordingly, it is concluded that the cold wall condition can enhance all four events in the near-wall region, and the increase of the Q2 (ejection) and Q3 (inward) events are larger than the Q1 (outward) and Q4 (sweep) events.

Joint PDFs of normalized streamwise fluctuation  $u''/u''_{\text{rms}}$  and normalized wall-normal fluctuation  $v''/v''_{\text{rms}}$  at four wall-normal locations  $y^+ = 10, 30, 50$ , and  $150$  (shown by dash-dot lines in Fig. 7)



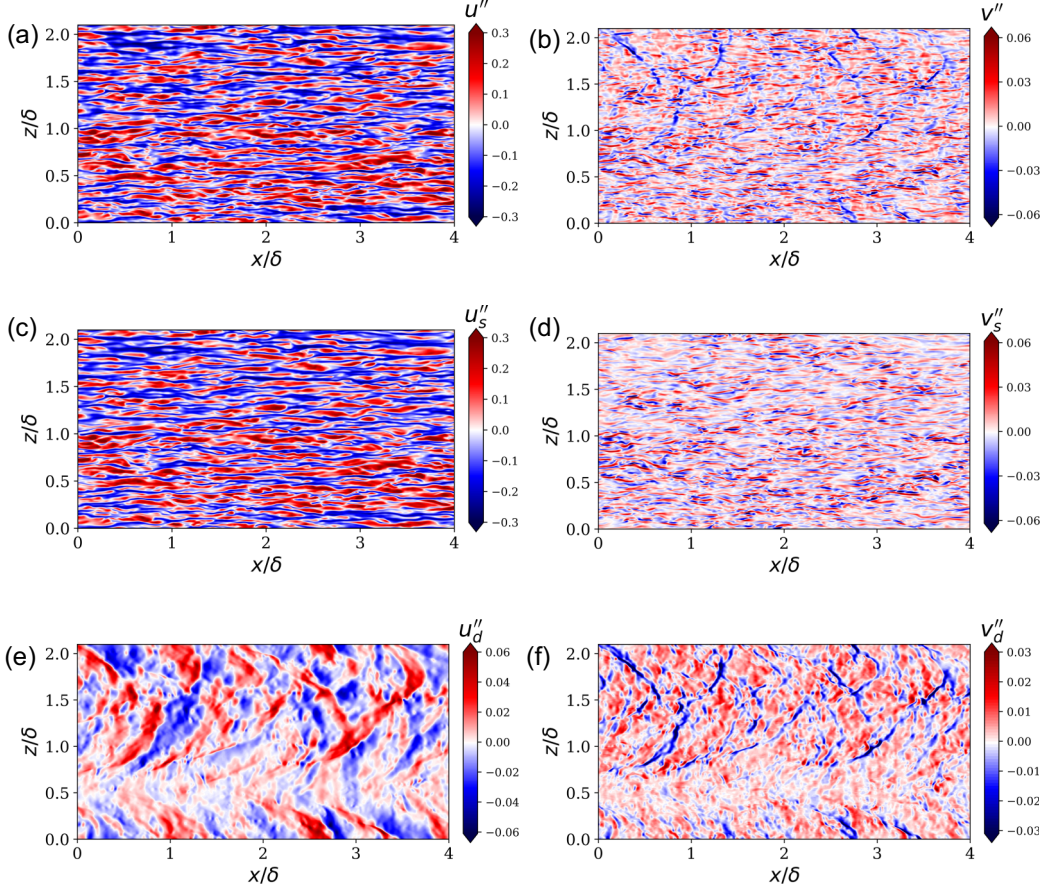


FIG. 6. Instantaneous fields of (a)  $u''$ , (b)  $v''$ , (c)  $u''_s$ , (d)  $v''_s$ , (e)  $u''_d$ , and (f)  $v''_d$  in a wall-parallel plane at  $y^+ = 10$  in M8T2.  $\delta$  is the boundary layer thickness.

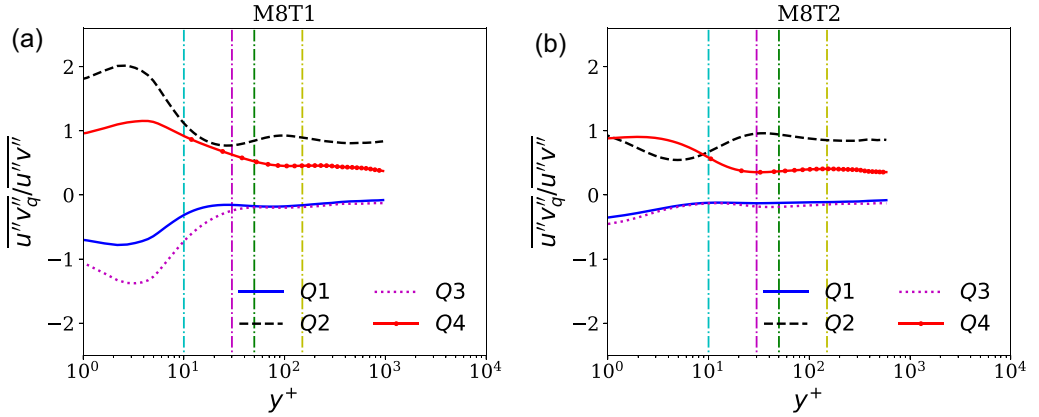


FIG. 7. Quadrant contributions to the turbulent shear stress along the wall-normal direction in (a) M8T1 and (b) M8T2. The dash-dot lines from left to right represent position  $y^+ = 10, 30, 50$ , and  $150$ , respectively.

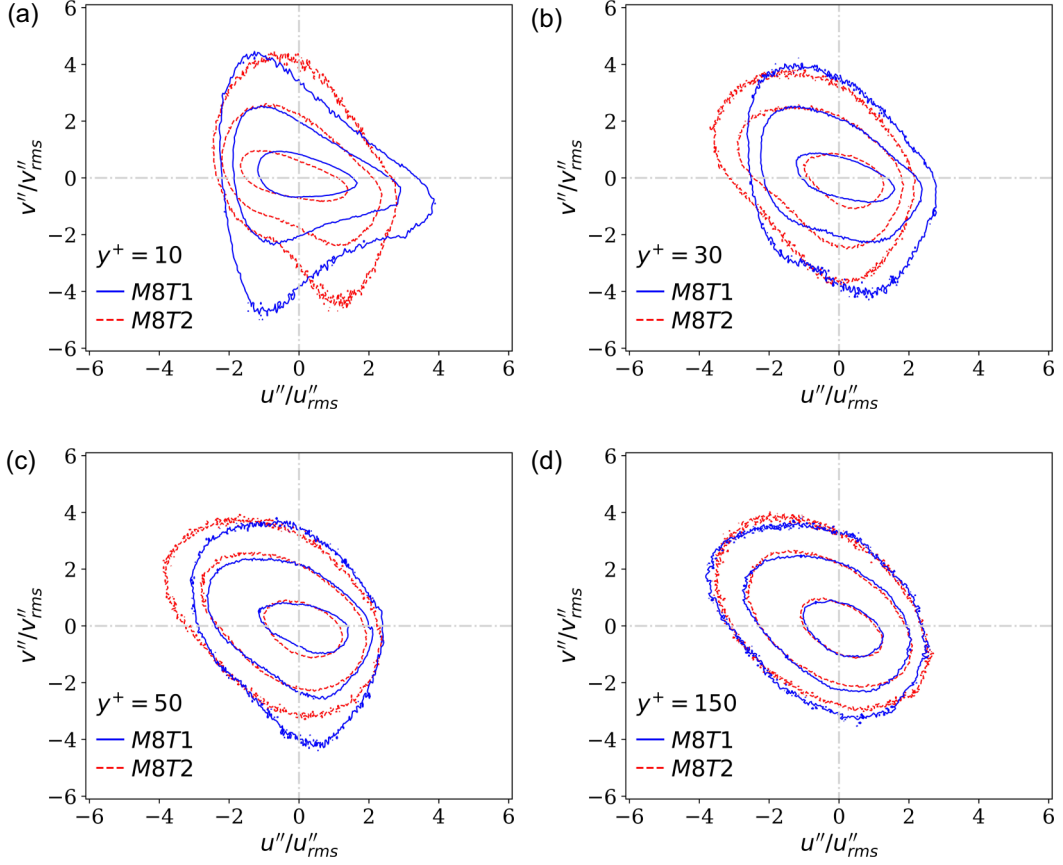


FIG. 8. Joint PDF of normalized streamwise fluctuation  $u''/u''_{rms}$  and normalized wall-normal fluctuation  $v''/v''_{rms}$  at (a)  $y^+ = 10$ , (b)  $y^+ = 30$ , (c)  $y^+ = 50$ , and (d)  $y^+ = 150$ . The contour levels 0.001, 0.01, 0.1, are shown.

are plotted in Fig. 8. It is found that joint PDFs at  $y^+ = 150$  are much wider in the second and fourth quadrants, and the second and fourth quadrants give the main contributions to the turbulent shear stress (shown by the yellow dash-dot line in Fig. 7), which indicates that Q2 (ejection) and Q4 (sweep) events are dominant far from the wall. In the near-wall region ( $y^+ = 10$ ), the Q3 (inward) event in M8T1 is much larger than that in M8T2, indicating that the cold wall condition enhances the inward event. This phenomenon is consistent with previous observation [Figs. 2(c) and 2(d)] that the cold wall enhances the compression motion near the wall. As the wall-normal location  $y^+$  increases, joint PDFs of  $u''/u''_{rms}$  and  $v''/v''_{rms}$  become more similar between M8T1 and M8T2, implying that the influence of the cold wall condition on the distribution of the normalized turbulent shear stress  $R_{uv}^+$  is focused on the near-wall region.

Quadrant contributions to the turbulent shear stress along the wall-normal direction conditioned on the normalized dilatation  $\theta''^+$  are depicted in Fig. 9 to demonstrate the effect of compressibility on the normalized turbulent shear stress  $R_{uv}^+$ . It is found that the Q1 (outward) and Q2 (ejection) events are mainly located in the expansion region, while the Q3 (inward) and Q4 (sweep) events are primarily situated in the compression region near the wall. However, the distributions of these four events in compression and expansion regions are similar far from the wall. Joint PDFs of normalized streamwise fluctuation  $u''/u''_{rms}$  and normalized wall-normal fluctuation  $v''/v''_{rms}$  conditioned on the normalized dilatation  $\theta''^+$  at  $y^+ = 10, 150$  are shown in Fig. 10. It is shown that the joint PDF

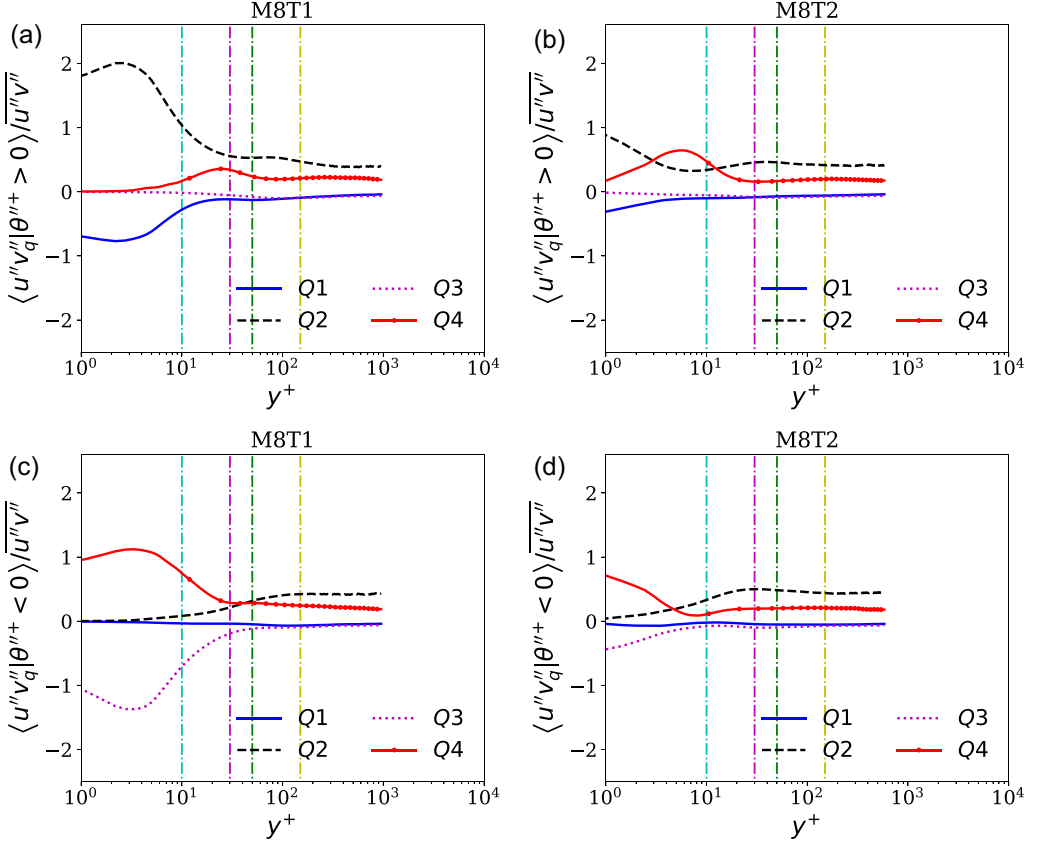


FIG. 9. Quadrant contributions to the turbulent shear stress along wall-normal direction conditioned on the normalized dilatation  $\theta''^+$ . (a)  $\theta''^+ > 0$  in M8T1; (b)  $\theta''^+ > 0$  in M8T2; (c)  $\theta''^+ < 0$  in M8T1; (d)  $\theta''^+ < 0$  in M8T2. The dash-dot lines from left to right represent position  $y^+ = 10, 30, 50$ , and  $150$ , respectively.

of M8T1 in Fig. 10(a) is mainly located in the first and second quadrants, while the joint PDF of M8T1 in Fig. 10(b) is primarily located in the third and fourth quadrants, which indicates that in M8T1, the positive  $v''$  events are dominant in the expansion region, while the negative  $v''$  events are primary in the compression region near the wall ( $y^+ = 10$ ). However, the joint PDFs in compression and expansion regions are similar far from the wall ( $y^+ = 150$ ), indicating that the compressibility effect on these four events is mainly in the near-wall region. It is also found that the joint PDFs of M8T2 are similar between the compression and expansion regions, indicating that the compression and expansion motions have a subtle influence on the distributions of four events in M8T2 due to weak compressibility compared with M8T1.

Conditional average  $\langle M_{uv}^+ | \theta''^+ \rangle$  of the tensor  $M_{uv}^+$  along the wall-normal direction is shown in Fig. 11. The dash-dot lines from left to right represent position  $y^+ = 10, 30, 50$ , and  $150$ , respectively. The data in the large magnitude of normalized dilatation  $|\theta''^+|$  are quite scattered due to lack of samples. It is revealed that the compressibility effect on  $\langle M_{uv}^+ | \theta''^+ \rangle$  is more prominent in M8T1 than in M8T2. In M8T1, it is found that strong positive values of  $\langle M_{uv}^+ | \theta''^+ \rangle$  appear in the compression region for  $5 < y^+ < 30$ , due to the fact that the Q3 (inward) event plays a central role in the compression region. Strong negative values of  $\langle M_{uv}^+ | \theta''^+ \rangle$  exist in the expansion region for  $10 < y^+ < 100$ , since the Q2 (ejection) event is dominant in the expansion region. At  $y^+ > 50$ , strong negative  $\langle M_{uv}^+ | \theta''^+ \rangle$  accumulates in the weak compression region, which can be attributed

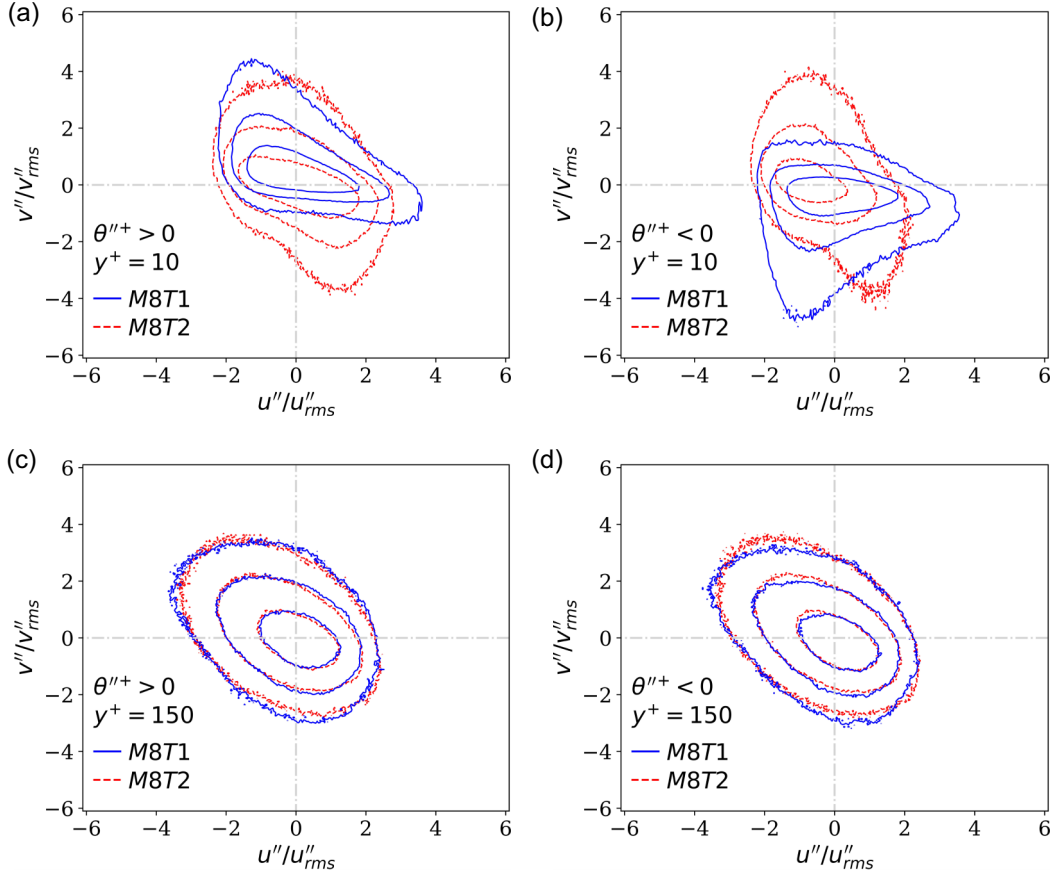


FIG. 10. Joint PDF of normalized streamwise fluctuation  $u''/u''_{rms}$  and normalized wall-normal fluctuation  $v''/v''_{rms}$  conditioned on the normalized dilatation  $\theta''^+$ . (a)  $\theta''^+ > 0$  at  $y^+ = 10$ ; (b)  $\theta''^+ < 0$  at  $y^+ = 10$ ; (c)  $\theta''^+ > 0$  at  $y^+ = 150$ ; (d)  $\theta''^+ < 0$  at  $y^+ = 150$ . The contour levels 0.001, 0.01, 0.05 are shown.

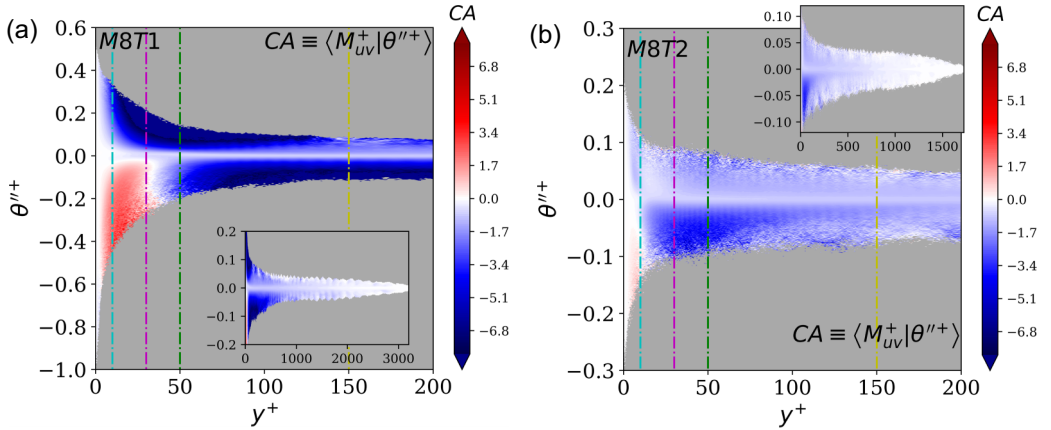


FIG. 11. The average of the tensor  $M_{uv}^+$  conditioned on the normalized dilatation  $\langle M_{uv}^+ | \theta''^+ \rangle$  along the wall-normal direction in (a) M8T1 and (b) M8T2. The dash-dot lines from left to right represent position  $y^+ = 10, 30, 50$ , and  $150$ , respectively.

to the domination of the Q2 (ejection) event and the Q4 (sweep) event in this region. Relative large negative values of the conditional average of  $M_{uv}^+$  exist in the large magnitude of normalized dilatation, implying that the Q2 (ejection) event and Q4 (sweep) event are highly correlated with the strong expansion region and strong compression region, respectively. Nevertheless, in M8T2, strong negative  $\langle M_{uv}^+ | \theta''^+ \rangle$  gathers in the weak compression region at  $10 < y^+ < 100$ , due to the strong Q2 (ejection) event and Q4 (sweep) event in this region. Other regions reveal the almost balance between positive and negative  $M_{uv}^+$ , indicating a weak correlation between dilatation and  $M_{uv}^+$  with high wall temperature. Accordingly, it is concluded that the effect of wall temperature has significant influence on  $\langle M_{uv}^+ | \theta''^+ \rangle$  only near the wall. In the near-wall region, wall temperature significantly affects four events. The compression motion is closely associated with the Q3 (inward) event, pumping low-speed fluid toward the wall. The expansion motion is highly associated with the Q2 (ejection) event, which has the main contribution to the negative values of  $R_{uv}$ . It is also found that the range of the normalized dilatation  $\theta''^+$  is much wider in M8T1 compared with that in M8T2, and the r.m.s. of the normalized dilatation  $\langle (\theta''^+)^2 \rangle^{1/2}$  is much larger in M8T1 than that in M8T2 near the wall [shown in Fig. 2(b)], indicating a stronger compressibility in M8T1. Accordingly, the above observations suggest that the cold wall drastically increases the compressibility near the wall and also enhances the Q3 (inward) event in compression region and Q2 (ejection) event in the expansion region. However, in the far-wall region, the Q2 (ejection) and Q4 (sweep) events dominate, which results in the negative values of  $R_{uv}$ . The local compressibility has a subtle influence on the distribution of four events far from the wall.

On the basis of Helmholtz decomposition, the joint PDFs of four decomposed components of the tensor  $M_{uv}^+$  at four wall-normal locations,  $y^+ = 10, 30, 50$ , and  $150$ , are depicted in Figs. 12–15, and the conditional averages of these decomposed components are plotted in Figs. 16 and 17.

Compared with Figs. 8 and 12, it is found that the joint PDF of  $u_s''/u_{s,rms}''$  and  $v_s''/v_{s,rms}''$  and the joint PDF of  $u''/u_{rms}''$  and  $v''/v_{rms}''$  are similar in M8T1 and M8T2 except for the near-wall region ( $y^+ = 10$ ) in M8T1, where a wider Q4 distribution and a narrower Q3 distribution appear in joint PDF of  $u_s''/u_{s,rms}''$  and  $v_s''/v_{s,rms}''$ , which shows the dominance of the Q2 and Q4 events in the joint PDF of  $u_s''/u_{s,rms}''$  and  $v_s''/v_{s,rms}''$  in M8T1. The joint PDFs of  $u_s''/u_{s,rms}''$  and  $v_s''/v_{s,rms}''$  in M8T1 and M8T2 become more and more similar as  $y^+$  increases, implying that the influence of the cold wall condition on the distribution of  $M_{u_s v_s}^+$  is negligibly small far from the wall. Compared with Figs. 11 and 16(a) and 16(b), it is found that the negative values of  $\langle M_{uv}^+ | \theta''^+ \rangle$  in the weak compression region at  $y^+ > 50$  in M8T1 and  $10 < y^+ < 100$  in M8T2 are mainly contributed by the Q2 event and Q4 event of the solenoidal component  $M_{u_s v_s}^+$ . Furthermore, in M8T1, the weak positive values of  $\langle M_{u_s v_s}^+ | \theta''^+ \rangle$  appear in the compression region at  $y^+ < 20$ , due to the weak positive correlation of  $u_s''$  and  $v_s''$ . Expansion motions at  $10 < y^+ < 100$  have the main contribution to the negative values of  $\langle M_{uv}^+ | \theta''^+ \rangle$ , which is induced by a negative correlation of  $u_s''$  and  $v_s''$ . Compared with  $\langle M_{u_s v_s}^+ | \theta''^+ \rangle$  in M8T1 and M8T2, the wall temperature has negligible influence on  $\langle M_{u_s v_s}^+ | \theta''^+ \rangle$ . The Q2 and Q4 events dominate far from the wall and are rarely influenced by local compressibility. In the near-wall region, the positive and negative values of  $M_{u_s v_s}^+$  are almost balanced.

It is shown in Fig. 13 that strong positive skewness of  $v_d''$  appears in M8T2, while a weak negative skewness of  $v_d''$  exists in M8T1. The  $u_d''$  exhibits weak negative skewness in M8T1 and M8T2, and the distributions of  $u_d''$  in both cases are similar. These observations indicate that the cold wall condition has a strong influence on the dilatational wall-normal fluctuation  $v_d''$ , which enhances the negative values of the dilatational wall-normal fluctuation  $v_d''$ , but has negligible effect on the dilatational streamwise fluctuation  $u_d''$ . It is depicted in Figs. 16(c) and 16(d) that in M8T1, relatively strong negative values of  $\langle M_{u_d v_d}^+ | \theta''^+ \rangle$  appear in the compression region at  $y^+ < 10$ , induced by the strong negative correlation between  $u_d''$  and  $v_d''$ . Relatively strong positive values of  $\langle M_{u_d v_d}^+ | \theta''^+ \rangle$  appear in the expansion region at  $10 < y^+ < 50$ , due to the strong positive correlation between  $u_d''$  and  $v_d''$ . At the far-wall region, the magnitudes of  $u_d''$  and  $v_d''$  are very small, giving rise to that

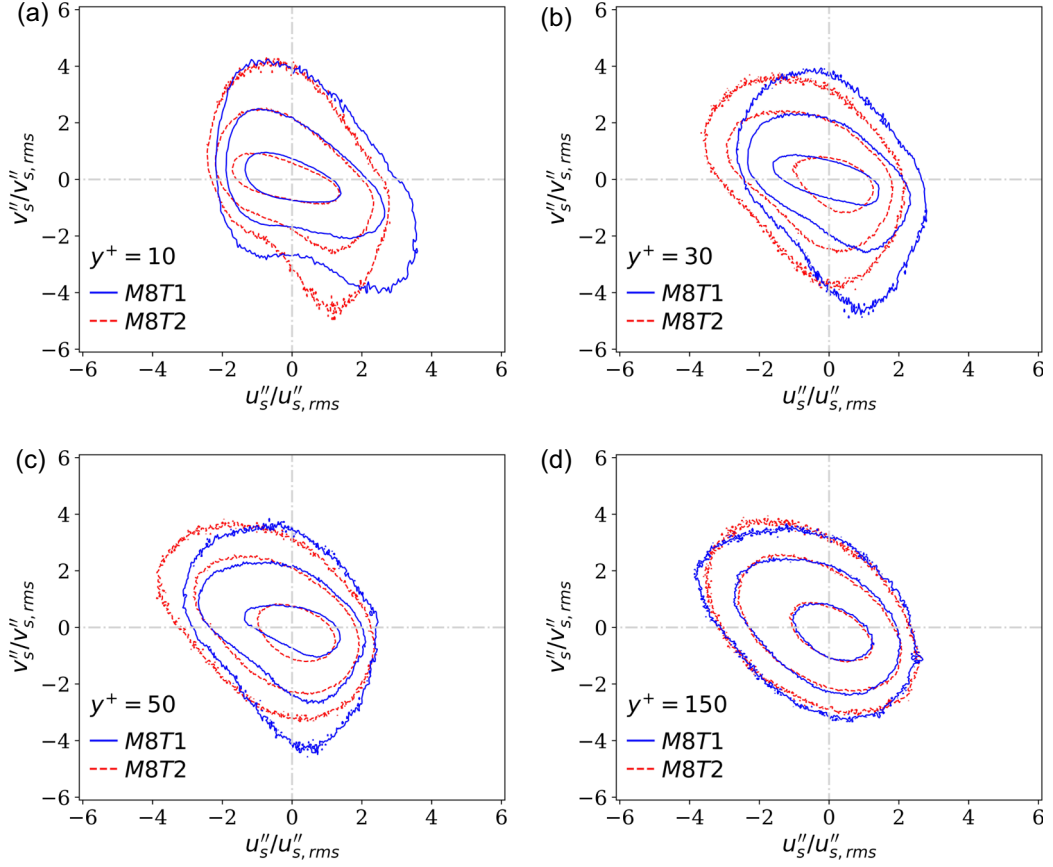


FIG. 12. Joint PDF of normalized streamwise solenoidal fluctuation  $u_s''/u_{s,rms}''$  and normalized wall-normal solenoidal fluctuation  $v_s''/v_{s,rms}''$  at (a)  $y^+ = 10$ , (b)  $y^+ = 30$ , (c)  $y^+ = 50$ , and (d)  $y^+ = 150$ . The contour levels 0.001, 0.01, 0.1 are shown.

$\langle M_{u_d v_d}^+ | \theta''^+ \rangle$  is nearly zero. In M8T2,  $\langle M_{u_d v_d}^+ | \theta''^+ \rangle$  is very small in the full region mainly due to weak compressibility.

It is depicted in Fig. 14 that the joint PDF of  $u_s''/u_{s,rms}''$  and  $v_d''/v_{d,rms}''$  shows no evidence of correlation for negative  $u_s''$  events, but exhibits strong positive correlation between positive  $u_s''$  and positive  $v_d''$  in M8T2. However, in M8T1, the behavior is totally different. A wider distribution of PDF of  $v_d''/v_{d,rms}''$  exists in the negative  $u_s''$  events near the wall in M8T1, indicating a strong positive correlation between negative  $u_s''$  and  $v_d''$ . It is also found that stronger negative  $u_s''$  events appear in M8T2 and stronger positive  $u_s''$  events exist in M8T1 near the wall, implying that the cold wall condition enhances the positive  $u_s''$  events and suppresses the negative  $u_s''$  events. It is shown in Figs. 17(a) and 17(b) that in M8T1, strong positive values of  $\langle M_{u_s v_d}^+ | \theta''^+ \rangle$  appear in the compression region at  $5 < y^+ < 30$  and strong negative values of  $\langle M_{u_s v_d}^+ | \theta''^+ \rangle$  exist in the expansion region at  $10 < y^+ < 50$ , which are the main contributions of the positive values of  $\langle M_{uv}^+ | \theta''^+ \rangle$  in the compression region and the negative values of  $\langle M_{uv}^+ | \theta''^+ \rangle$  in the expansion region, respectively. The positive values of  $\langle M_{u_s v_d}^+ | \theta''^+ \rangle$  in the compression region are mainly caused by the Q3 event, and the negative values of  $\langle M_{u_s v_d}^+ | \theta''^+ \rangle$  in the expansion region are mainly due to the Q2 event. In M8T2, weak positive values appear in the strong compression region. Compared with  $\langle M_{u_s v_d}^+ | \theta''^+ \rangle$  in M8T1 and M8T2, wall temperature has a significant influence on distribution of four events of  $u_s''$  and  $v_d''$ .



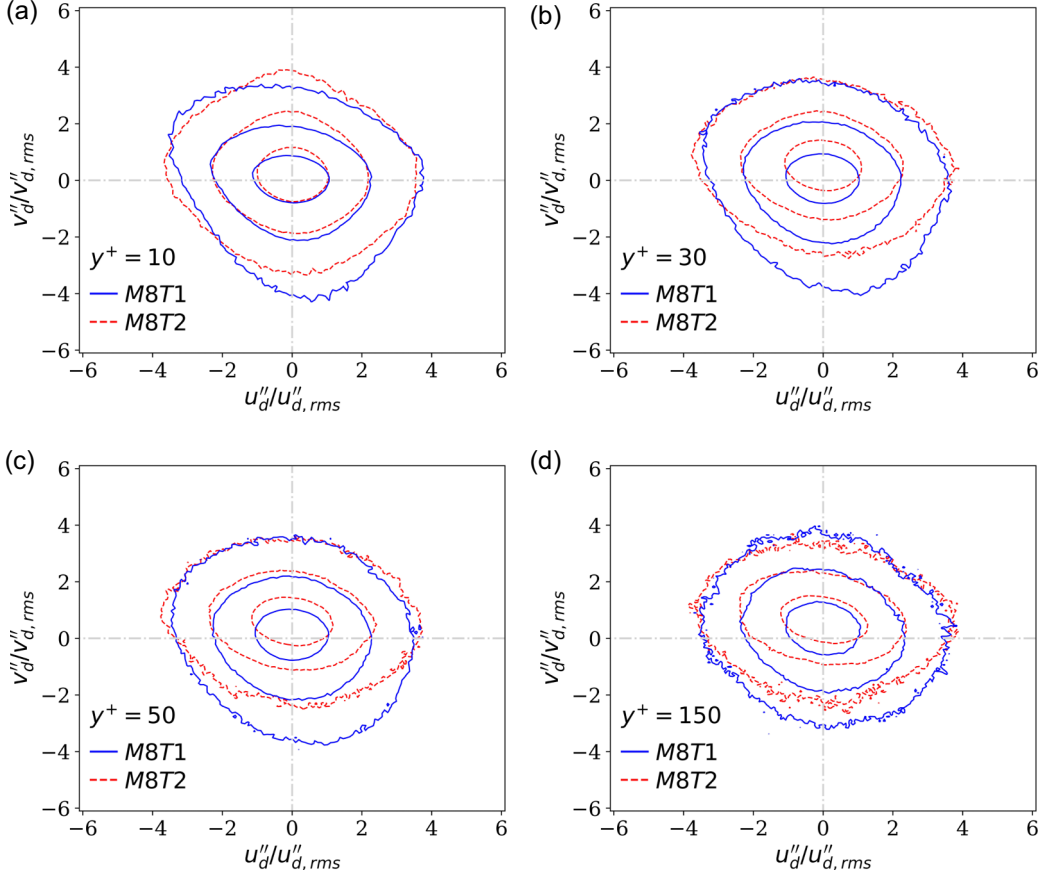


FIG. 13. Joint PDF of normalized streamwise dilatational fluctuation  $u_d''/u_{d,rms}''$  and normalized wall-normal dilatational fluctuation  $v_d''/v_{d,rms}''$  at (a)  $y^+ = 10$ , (b)  $y^+ = 30$ , (c)  $y^+ = 50$ , and (d)  $y^+ = 150$ . The contour levels 0.001, 0.01, 0.1 are shown.

near the wall. The cold wall drastically enhances Q3 event in the compression region and Q2 event in the expansion region. The term  $\langle M_{u_s v_d}^+ | \theta''^+ \rangle$  is the main reason for the difference of  $\langle M_{uv}^+ | \theta''^+ \rangle$  in M8T1 and M8T2 near the wall. However, in the far-wall region,  $\langle M_{u_s v_d}^+ | \theta''^+ \rangle$  is almost zero in both M8T1 and M8T2, mainly due to weak compressibility in this region.

It is shown in Fig. 15 that the joint PDFs of  $u_d''/u_{d,rms}''$  and  $v_s''/v_{s,rms}''$  in M8T1 and M8T2 are similar except for a slightly larger distribution at large negative  $v_s''$  events in M8T1, indicating that the cold wall condition has negligible influence on the  $u_d''$  and  $v_s''$ . It is depicted in Figs. 17(c) and 17(d) that the cold wall has a negligible effect on  $\langle M_{u_d v_s}^+ | \theta''^+ \rangle$ , which is consistent with the fact that  $R_{u_d v_s}^+$  is nearly independent of the wall temperature. Moreover,  $\langle M_{u_d v_s}^+ | \theta''^+ \rangle$  gives rare contribution to  $\langle M_{uv}^+ | \theta''^+ \rangle$ .

Consequently, it is concluded that among four decomposed components,  $\langle M_{u_s v_s}^+ | \theta''^+ \rangle$  and  $\langle M_{u_s v_d}^+ | \theta''^+ \rangle$  are the main contributions to  $\langle M_{uv}^+ | \theta''^+ \rangle$ .  $\langle M_{u_s v_s}^+ | \theta''^+ \rangle$  is nearly independent of the wall temperature and gives the main contribution to  $\langle M_{uv}^+ | \theta''^+ \rangle$  far from the wall. On the other hand,  $M_{u_s v_d}^+$  is drastically affected by wall temperature and dominant in  $\langle M_{uv}^+ | \theta''^+ \rangle$  near the wall. Other two components give little contribution to  $\langle M_{uv}^+ | \theta''^+ \rangle$ . The cold wall can drastically enhance  $\langle M_{u_d v_d}^+ | \theta''^+ \rangle$  near the wall, while  $\langle M_{u_d v_s}^+ | \theta''^+ \rangle$  is nearly irrelevant with the wall temperature.



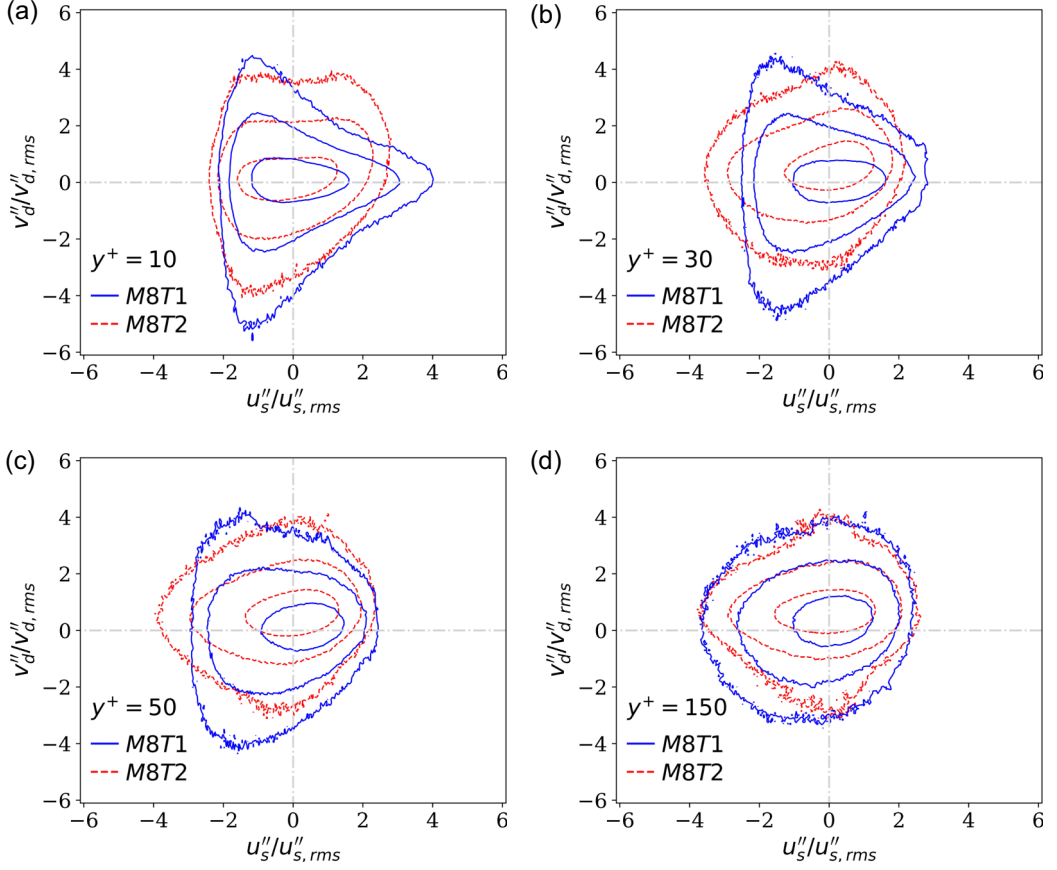


FIG. 14. Joint PDF of normalized streamwise solenoidal fluctuation  $u_s''/u_{s,rms}''$  and normalized wall-normal dilatational fluctuation  $v_d''/v_{d,rms}''$  at (a)  $y^+ = 10$ , (b)  $y^+ = 30$ , (c)  $y^+ = 50$ , and (d)  $y^+ = 150$ . The contour levels 0.001, 0.01, 0.1 are shown.

## V. CORRELATIONS BETWEEN VELOCITY FLUCTUATIONS AND FLUCTUATING TEMPERATURE

The correlations between streamwise, wall-normal velocity fluctuations  $u''$ ,  $v''$ , and fluctuating temperature  $T'$  are often investigated to examine the SRA. The correlation coefficients between streamwise, wall-normal velocity fluctuations  $u''$ ,  $v''$ , and fluctuating temperature  $T'$  are defined as

$$C_{u''T'} \equiv \frac{\langle u''T' \rangle}{(\langle u''^2 \rangle \langle T'^2 \rangle)^{1/2}}, \quad C_{v''T'} \equiv \frac{\langle v''T' \rangle}{(\langle v''^2 \rangle \langle T'^2 \rangle)^{1/2}} \quad (18)$$

On the basis of Helmholtz decomposition, the correlation coefficients  $C_{u''T'}$  and  $C_{v''T'}$  can be decomposed into solenoidal and dilatational components, which can be expressed as

$$C_{u''T'} = \frac{\langle u_s''T' \rangle}{(\langle u''^2 \rangle \langle T'^2 \rangle)^{1/2}} + \frac{\langle u_d''T' \rangle}{(\langle u''^2 \rangle \langle T'^2 \rangle)^{1/2}} \equiv C_{u_s''T'}^* + C_{u_d''T'}^* \quad (19)$$

$$C_{v''T'} = \frac{\langle v_s''T' \rangle}{(\langle v''^2 \rangle \langle T'^2 \rangle)^{1/2}} + \frac{\langle v_d''T' \rangle}{(\langle v''^2 \rangle \langle T'^2 \rangle)^{1/2}} \equiv C_{v_s''T'}^* + C_{v_d''T'}^* \quad (20)$$

The correlation coefficients  $C_{u''T'}$ ,  $C_{v''T'}$  and their decomposed components along wall-normal direction are plotted in Fig. 18. It is revealed that the intersection points of  $C_{u''T'}$  and  $C_{v''T'}$  with

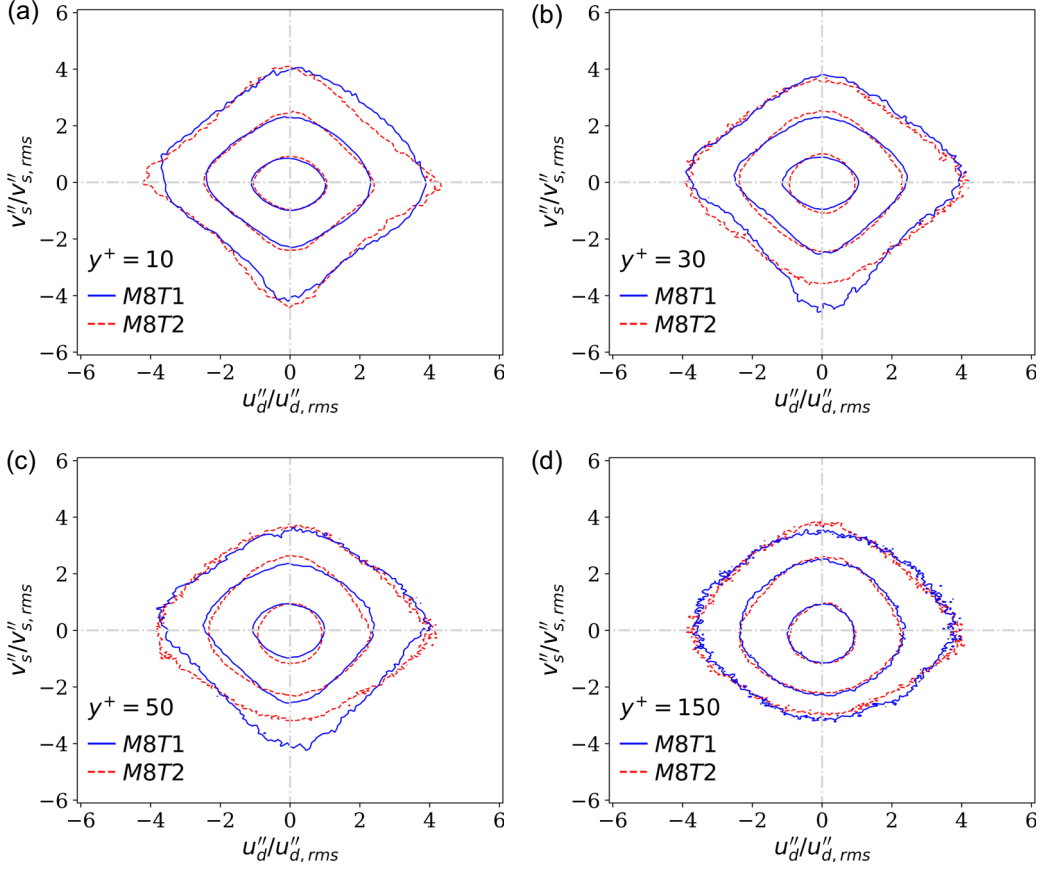


FIG. 15. Joint PDF of normalized streamwise dilatational fluctuation  $u_d''/u_{d,rms}''$  and normalized wall-normal solenoidal fluctuation  $v_s''/v_{s,rms}''$  at (a)  $y^+ = 10$ , (b)  $y^+ = 30$ , (c)  $y^+ = 50$ , and (d)  $y^+ = 150$ . The contour levels 0.001, 0.01, 0.1 are shown.

$C = 0$  move farther away from the wall as the wall temperature decreases, which is consistent with Ref. [4]. This partially due to the farther location of the maximum mean temperature  $\langle T \rangle$  [4], as is shown in the inset of Fig. 18(a). The strong correlation of  $u''$  and  $T'$  near the wall is found in M8T1, while  $u''$  and  $T'$  in M8T2 are slightly positively correlated in the near-wall region. It is shown that the cold wall drastically enhances the positive correlation between  $u''$  and  $T'$  near the wall. As the wall-normal distance increases,  $C_{u''T'}$  becomes negative. The value of  $C_{u''T'}$  tends to be nearly  $-0.67$  far from the wall, similar to the results reported in Refs. [4,13,21]. However,  $C_{u''T'}$  far from the wall in M8T1 is slightly larger than that in M8T2, indicating that the cold wall slightly weakens the negative correlation of  $u''$  and  $T'$  far from the wall. The strong positive correlation between  $u''$  and  $T'$  in M8T1 is mainly caused by the dilatational component of streamwise velocity fluctuation  $u_d''$  near the wall. The dominance of  $C_{u_d''T'}$  in  $C_{u''T'}$  is significantly enhanced by the cold wall. However, the values of  $C_{u''T'}$  and  $C_{u_s''T'}$  are coincident far from the wall in M8T1 and M8T2, implying that the correlation between  $u''$  and  $T'$  is mainly dominated by the solenoidal component of streamwise velocity fluctuation  $u_s''$  far from the wall.

It is depicted that  $v''$  and  $T'$  are negatively correlated near the wall, and the negative correlation is weaker in M8T1, indicating that the cold wall suppresses the negative correlation between  $v''$  and  $T'$  near the wall. As wall-normal distance increases,  $C_{v''T'}$  becomes positive. The value of  $C_{v''T'}$  tends to be nearly 0.47 far from the wall, which is similar to the observation reported in Ref. [13].

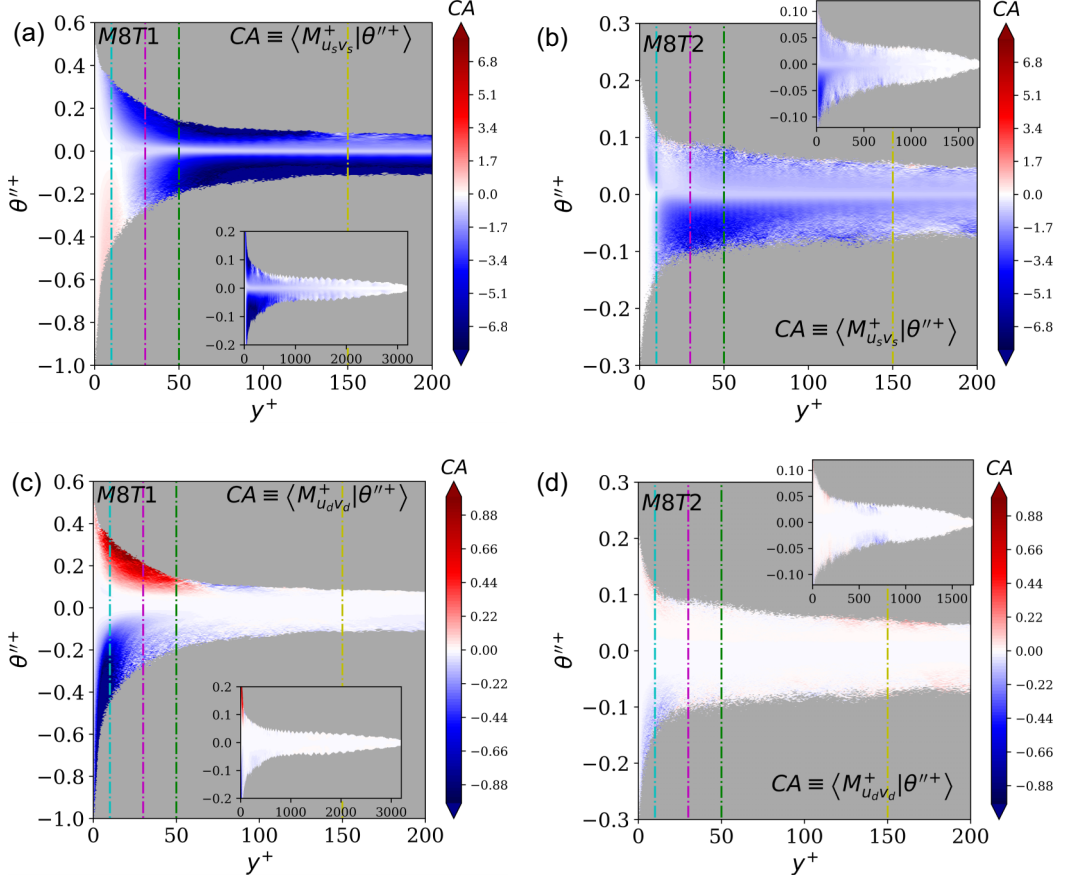


FIG. 16. The average of solenoidal and dilatational components of the tensor  $M_{u_s v_s}^+$  and  $M_{u_d v_d}^+$  conditioned on the normalized dilatation  $\langle M_{u_s v_s}^+ | \theta''^+ \rangle$  and  $\langle M_{u_d v_d}^+ | \theta''^+ \rangle$  along the wall-normal direction. (a)  $\langle M_{u_s v_s}^+ | \theta''^+ \rangle$  in M8T1; (b)  $\langle M_{u_s v_s}^+ | \theta''^+ \rangle$  in M8T2; (c)  $\langle M_{u_d v_d}^+ | \theta''^+ \rangle$  in M8T1; (d)  $\langle M_{u_d v_d}^+ | \theta''^+ \rangle$  in M8T2. The dash-dot lines from left to right represent position  $y^+ = 10, 30, 50, 150$ , respectively.

$C_{v''T'}$  far from the wall in M8T1 is slightly smaller than that in M8T2, indicating that the cold wall slightly weakens the positive correlation of  $v''$  and  $T'$  far from the wall. The negative correlations between  $v''$  and  $T'$  in M8T1 and M8T2 are mainly contributed by the dilatational component of wall-normal velocity fluctuation  $v_d''$  near the wall, and the cold wall suppresses the dominance of  $C_{v_d''T'}^*$  in  $C_{v''T'}$ . However, the values of  $C_{v''T'}$  and  $C_{v_s''T'}^*$  are coincident in M8T1 and M8T2 far from the wall, implying that the correlation between  $v''$  and  $T'$  is mainly dominated by the solenoidal component of wall-normal velocity fluctuation  $v_s''$  far from the wall.

Accordingly, it is concluded that the cold wall can enhance the positive correlation between  $u''$  and  $T'$  and suppress the negative correlation between  $v''$  and  $T'$  near the wall, which are closely related with the previous observations in Figs. 5 and 6 that the cold wall can increase the streamwise coherency of near-wall streaks and suppress spotty structures. However, the cold wall slightly weakens the negative correlation of  $u''$  and  $T'$  and the positive correlation of  $v''$  and  $T'$ , respectively, far from the wall.  $C_{u''T'}$  and  $C_{v''T'}$  are mainly contributed by their dilatational components near the wall, and dominated by their solenoidal components far from the wall.

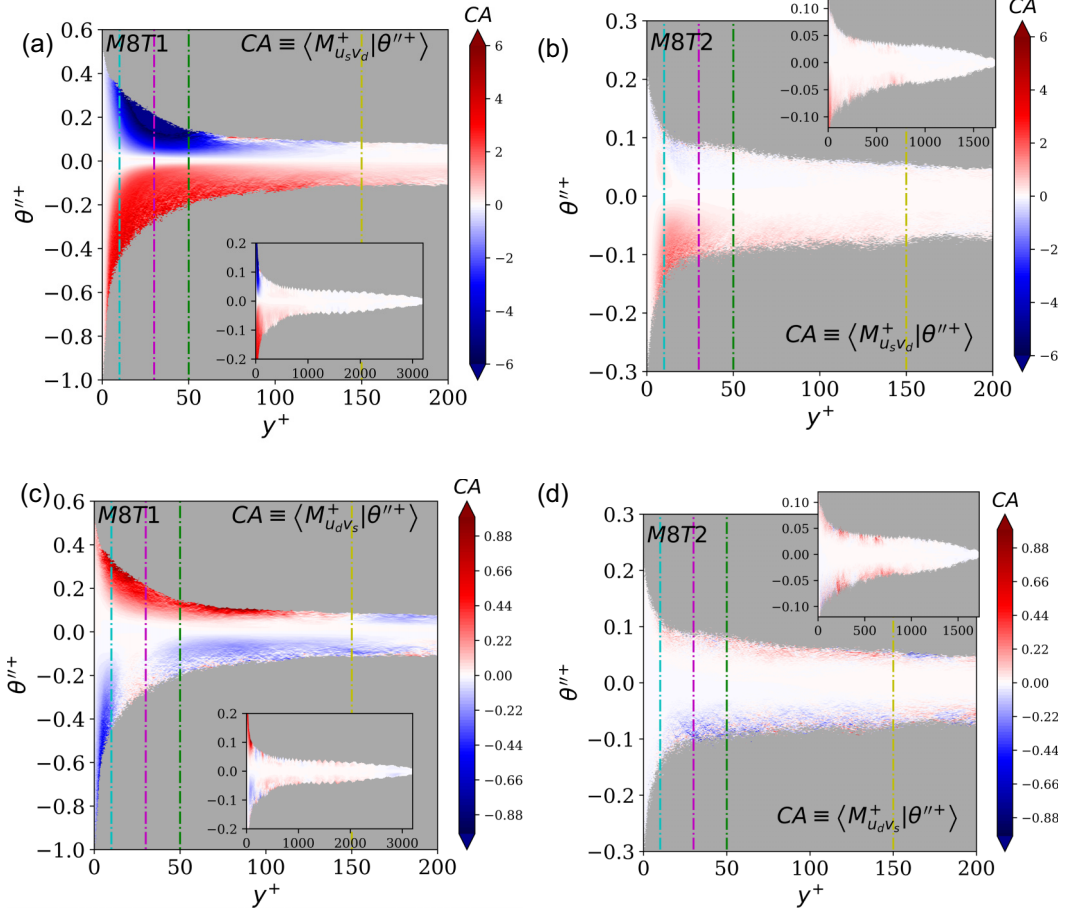


FIG. 17. The average of solenoidal-dilatational and dilatational-solenoidal components of the tensor  $M_{u_s v_d}^+$  and  $M_{u_d v_s}^+$  conditioned on the normalized dilatation  $\langle M_{u_s v_d}^+ | \theta''^+ \rangle$  and  $\langle M_{u_d v_s}^+ | \theta''^+ \rangle$  along the wall-normal direction. (a)  $\langle M_{u_s v_d}^+ | \theta''^+ \rangle$  in M8T1; (b)  $\langle M_{u_s v_d}^+ | \theta''^+ \rangle$  in M8T2; (c)  $\langle M_{u_d v_s}^+ | \theta''^+ \rangle$  in M8T1; (d)  $\langle M_{u_d v_s}^+ | \theta''^+ \rangle$  in M8T2. The dash-dot lines from left to right represent position  $y^+ = 10, 30, 50$ , and  $150$ , respectively.

## VI. THE KINETIC AND INTERNAL ENERGY BUDGETS

With the introduction of a new variable  $\phi \equiv \sqrt{e} = \sqrt{\frac{p}{\gamma-1}}$ , Mittal and Girimaji [54] developed a mathematical framework of the energy exchange in kinetic and internal energy. The velocity field is decomposed into a Favre average and a corresponding fluctuation field,  $\mathbf{u} = \mathbf{U} + \mathbf{u}'$ . Other variables  $\psi$  (such as pressure  $p$  and temperature  $T$ ) are decomposed using Reynolds averaging,  $\psi = \bar{\psi} + \psi'$ . Thus, the mean kinetic and internal energy  $\bar{K}$  and  $\bar{e}$  can be expressed as [54]

$$\bar{K} = \frac{1}{2} \bar{\rho} \tilde{U}_i \tilde{U}_i + \frac{1}{2} \overline{\rho u_i'' u_i''} \equiv K_m + k, \quad (21)$$

$$\bar{e} = \bar{\phi}^2 = \bar{\phi} \bar{\phi} + \overline{\phi' \phi'} \equiv e_m + e_t, \quad (22)$$

where  $\phi$  is decomposed using Reynolds averaging  $\phi = \bar{\phi} + \phi'$ , which are expressed as

$$\bar{\phi} = \sqrt{\frac{P}{\gamma-1}}, \quad \phi' = \sqrt{\frac{P}{\gamma-1}} - \sqrt{\frac{P}{\gamma-1}}. \quad (23)$$

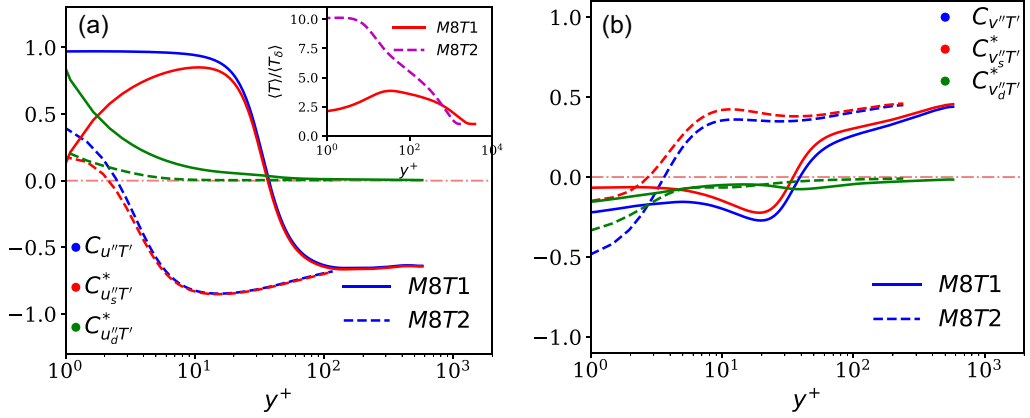


FIG. 18. The correlation coefficients (a)  $C_{u''T'}$ ,  $C_{u_s''T'}^*$ , and  $C_{u_d''T'}^*$ . Inset: the normalized mean temperature  $\langle T \rangle / \langle T_\delta \rangle$  along wall-normal direction. (b)  $C_{v''T'}$ ,  $C_{v_s''T'}^*$ , and  $C_{v_d''T'}^*$  along the wall-normal direction.

The equation for the mean field of kinetic energy ( $K_m$ ) is given by [54]

$$\begin{aligned} \frac{\partial K_m}{\partial t} + \frac{\partial(K_m \tilde{U}_j)}{\partial x_j} + \frac{\partial}{\partial x_j} [\overline{\rho u_i'' u_j''} \tilde{U}_i + \bar{p} \tilde{U}_j - \bar{\sigma}_{ij} \tilde{U}_i] \\ = \overline{\rho u_i'' u_j''} \frac{\partial \tilde{U}_i}{\partial x_j} + \bar{p} \frac{\partial \tilde{U}_k}{\partial x_k} - \bar{\sigma}_{ij} \frac{\partial \tilde{U}_i}{\partial x_j} + \overline{u_k''} \frac{\partial \bar{p}}{\partial x_k} - \overline{u_k''} \frac{\partial \bar{\sigma}_{kj}}{\partial x_j}. \end{aligned} \quad (24)$$

The equation for the fluctuating field of kinetic energy ( $k$ ) is given by [54]

$$\begin{aligned} \frac{\partial k}{\partial t} + \frac{\partial(k \tilde{U}_j)}{\partial x_j} + \frac{\partial}{\partial x_j} \left[ \frac{1}{2} \overline{\rho u_i'' u_i'' u_j''} + \overline{p' u_j''} - \overline{\sigma'_{ij} u_i''} \right] \\ = -\overline{\rho u_i'' u_j''} \frac{\partial \tilde{U}_i}{\partial x_j} + \overline{p' \frac{\partial u_k''}{\partial x_k}} - \overline{\sigma'_{ij} \frac{\partial u_i''}{\partial x_j}} - \overline{u_k''} \frac{\partial \bar{p}}{\partial x_k} + \overline{u_k''} \frac{\partial \bar{\sigma}_{kj}}{\partial x_j}. \end{aligned} \quad (25)$$

The mean and fluctuating pressure can be expressed in terms of the internal energy variable  $\phi$  as

$$\bar{p} = (\gamma - 1)[\bar{\phi} \bar{\phi} + \overline{\phi' \phi'}], \quad p' = (\gamma - 1)[\phi' \phi' + 2\bar{\phi} \phi' - \overline{\phi' \phi'}]. \quad (26)$$

Thus, the mean and fluctuating pressure can be divided into two components [54]

$$\bar{p} = \bar{p}_m + \bar{p}_t, \quad p' = p'_m + p'_t, \quad (27)$$

where

$$\bar{p}_m = (\gamma - 1) \bar{\phi} \bar{\phi}, \quad \bar{p}_t = (\gamma - 1) \overline{\phi' \phi'}, \quad (28)$$

$$p'_m = 2(\gamma - 1) \bar{\phi} \phi', \quad p'_t = (\gamma - 1) [\phi' \phi' - \overline{\phi' \phi'}]. \quad (29)$$

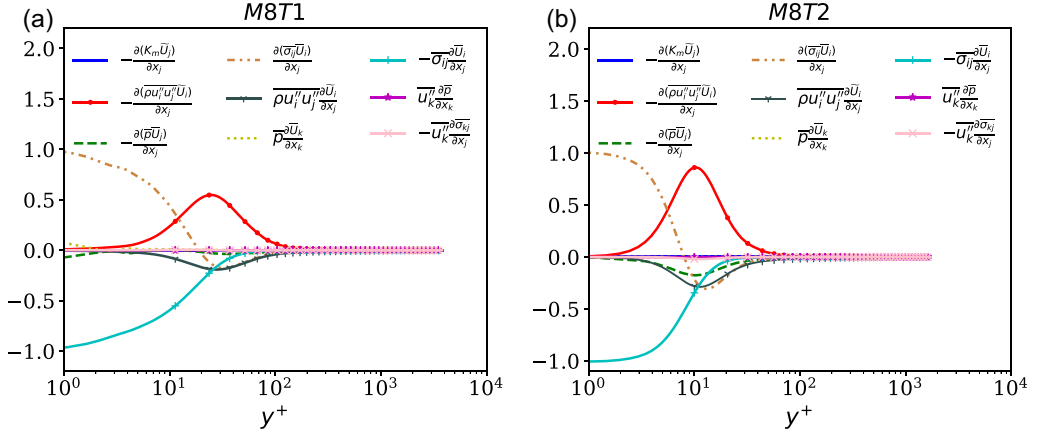


FIG. 19. The mean field of kinetic energy  $K_m$  budget along wall-normal direction in (a) M8T1 and (b) M8T2. All terms are normalized by  $\rho_w u_\tau^3 / \delta_v$ .

Thus, the equation for mean field of the internal energy ( $e_m$ ) is given by [54]

$$\begin{aligned} \frac{\partial e_m}{\partial t} + \frac{\partial(e_m \tilde{U}_k)}{\partial x_k} + \frac{\partial}{\partial x_k} [\bar{\phi} \bar{\phi}' u_k'' + 2\bar{\phi} \bar{\phi}' u_k'' + \bar{q}_k] \\ = \bar{\sigma}_{ij} \frac{\partial \tilde{U}_i}{\partial x_j} + \bar{\sigma}_{ij}' \frac{\partial u_i''}{\partial x_j} - \bar{p}_m \frac{\partial \tilde{U}_k}{\partial x_k} + 2\bar{u}_k'' \bar{\phi}' \frac{\partial \bar{\phi}}{\partial x_k} + \frac{2-\gamma}{2(\gamma-1)} \bar{p}_m' \frac{\partial u_k''}{\partial x_k} - \frac{\bar{f} \bar{\phi}'}{\bar{\phi}}. \end{aligned} \quad (30)$$

The equation for fluctuating field of the internal energy ( $e_t$ ) is given by [54]

$$\begin{aligned} \frac{\partial e_t}{\partial t} + \frac{\partial(e_t \tilde{U}_k)}{\partial x_k} + \frac{\partial(\bar{\phi}' \bar{\phi}' u_k'')}{\partial x_k} \\ = -\bar{p}_t' \frac{\partial \tilde{U}_k}{\partial x_k} - \bar{p}' \frac{\partial u_k''}{\partial x_k} - 2\bar{u}_k'' \bar{\phi}' \frac{\partial \bar{\phi}}{\partial x_k} - \frac{2-\gamma}{2(\gamma-1)} \bar{p}_m' \frac{\partial u_k''}{\partial x_k} + \frac{\bar{f} \bar{\phi}'}{\bar{\phi}}. \end{aligned} \quad (31)$$

Here the thermal flux is  $q_k = -\kappa \frac{\partial T}{\partial x_k}$  and  $\bar{f} = -\frac{\partial q_k}{\partial x_k} + \bar{\sigma}_{ij} \frac{\partial u_i}{\partial x_j}$  is the sum of the thermal flux and viscous terms.

The mean and fluctuating fields of kinetic and internal energy budgets of Eqs. (24), (25), (30), and (31) in M8T1 and M8T2 are shown in Figs. 19–22.

Then we discuss the energy exchanges among  $K_m$ ,  $k$ ,  $e_m$ , and  $e_t$ . First, the  $K_m$ - $k$  interactions are considered. The most important interaction between mean-turbulent kinetic energy is the production term  $-\overline{\rho u_i'' u_j'' \frac{\partial \tilde{U}_i}{\partial x_j}}$ . The production term  $-\overline{\rho u_i'' u_j'' \frac{\partial \tilde{U}_i}{\partial x_j}}$  and its decomposed components along wall-normal direction are shown in Fig. 23. It is shown that the production term  $-\overline{\rho u_i'' u_j'' \frac{\partial \tilde{U}_i}{\partial x_j}}$  plays a dominant role in  $K_m$ - $k$  interactions and is always positive, indicating that production term draws energy from the mean flow and deposits it into the fluctuating field. The production term  $-\overline{\rho u_i'' u_j'' \frac{\partial \tilde{U}_i}{\partial x_j}}$  achieves its peak in the buffer layer. The solenoidal component  $-\overline{\rho u_{s,i}'' u_{s,j}'' \frac{\partial \tilde{U}_i}{\partial x_j}}$  has the main contribution to the production term and even has a higher positive peak in the buffer layer compared with the production term. The term  $-\overline{\rho u_{s,i}'' u_{d,j}'' \frac{\partial \tilde{U}_i}{\partial x_j}}$  achieves its peak in the buffer layer and depletes the solenoidal component  $-\overline{\rho u_{s,i}'' u_{s,j}'' \frac{\partial \tilde{U}_i}{\partial x_j}}$ . In M8T1, the dilatational component  $-\overline{\rho u_{d,i}'' u_{d,j}'' \frac{\partial \tilde{U}_i}{\partial x_j}}$  achieves its peak near the wall and has a relatively small contribution to the production term. The term  $-\overline{\rho u_{d,i}'' u_{s,j}'' \frac{\partial \tilde{U}_i}{\partial x_j}}$  has negligible contribution to the production term. However, in M8T2 these two

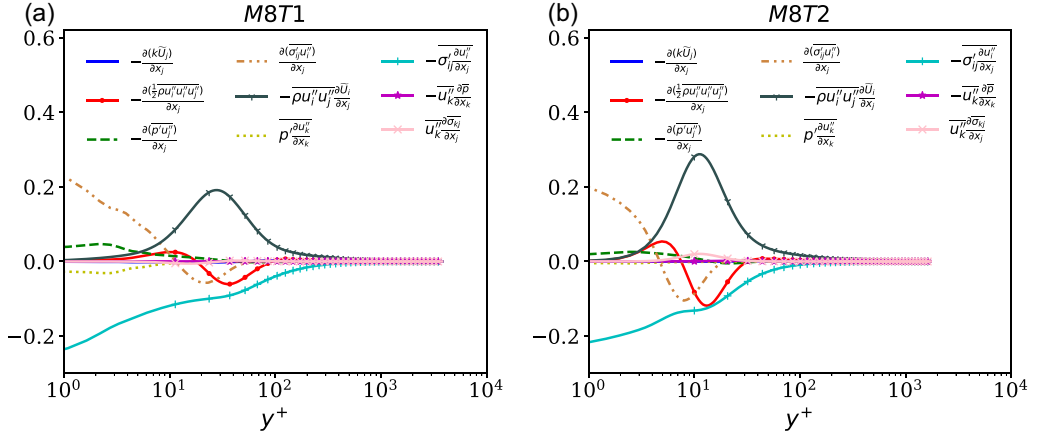


FIG. 20. The fluctuating field of kinetic energy  $k$  budget along the wall-normal direction in (a) M8T1 and (b) M8T2. All terms are normalized by  $\rho_w u_\tau^3 / \delta_v$ .

components  $-\overline{\rho u''_{d,i} u''_{d,j}} \frac{\partial \tilde{U}_j}{\partial x_j}$  and  $-\overline{\rho u''_{d,i} u''_{s,j}} \frac{\partial \tilde{U}_j}{\partial x_j}$  have negligible contributions to the production term due to weak compressibility. Another two interactions  $\overline{u''_k \frac{\partial \bar{p}}{\partial x_k}}$  and  $\overline{u''_k \frac{\partial \bar{\sigma}_{kj}}{\partial x_j}}$  are caused by pressure work and viscous action, respectively. The terms  $\overline{u''_k \frac{\partial \bar{p}}{\partial x_k}}$  and  $\overline{u''_k \frac{\partial \bar{\sigma}_{kj}}{\partial x_j}}$  along the wall-normal direction in M8T1 and M8T2 are shown in Figs. 24 and 25, respectively. It is found that the magnitudes of  $\overline{u''_k \frac{\partial \bar{\sigma}_{kj}}{\partial x_j}}$  and  $\overline{u''_k \frac{\partial \bar{p}}{\partial x_k}}$  are one and two orders smaller than that of the production term  $-\overline{\rho u''_i u''_j \frac{\partial \tilde{U}_j}{\partial x_j}}$ , respectively, indicating that these two interactions have negligible contributions to the interactions between  $K_m$  and  $k$ . It is noticed that the negative value of  $\overline{u''_k \frac{\partial \bar{p}}{\partial x_k}}$  represents the energy transfer from the mean flow to the fluctuating field and vice versa. It is shown in Fig. 24 that  $\overline{u''_k \frac{\partial \bar{p}}{\partial x_k}}$  is mainly governed by its dilatational component  $\overline{u''_{d,k} \frac{\partial \bar{p}}{\partial x_k}}$  in the buffer layer and far from the wall, except for the cancellation of solenoidal component  $\overline{u''_{s,k} \frac{\partial \bar{p}}{\partial x_k}}$  and dilatational component  $\overline{u''_{d,k} \frac{\partial \bar{p}}{\partial x_k}}$  in the near-wall region.  $\overline{u''_k \frac{\partial \bar{p}}{\partial x_k}}$  mainly transfers energy from mean flow to fluctuating field in the buffer layer, and weak reverse

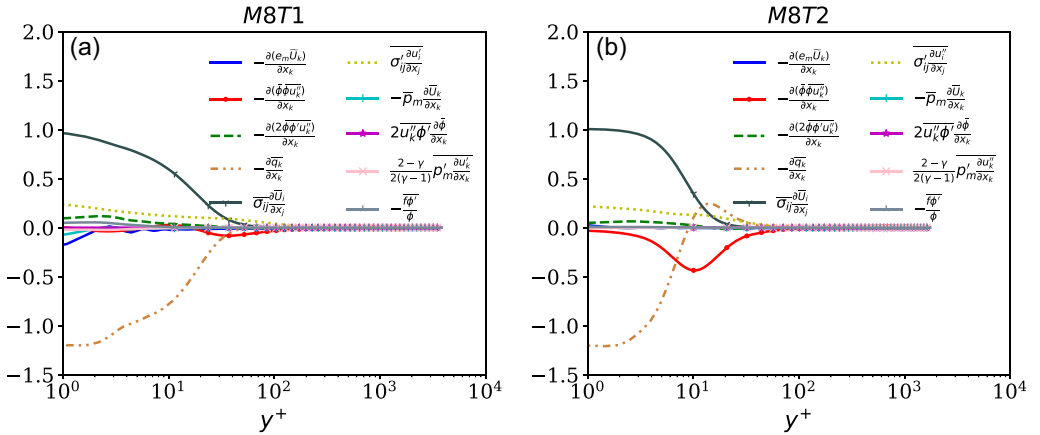


FIG. 21. The mean field of internal energy  $e_m$  budget along the wall-normal direction in (a) M8T1 and (b) M8T2. All terms are normalized by  $\rho_w u_\tau^3 / \delta_v$ .



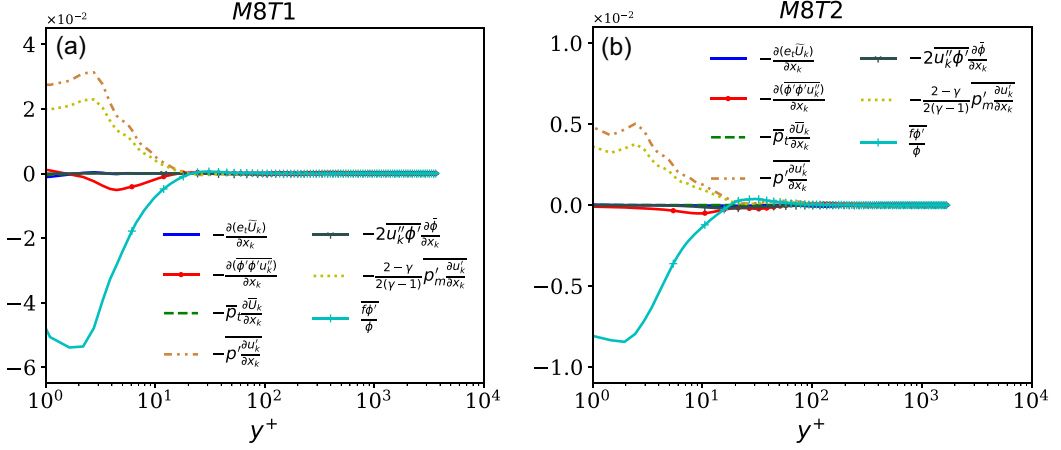


FIG. 22. The fluctuating field of internal energy  $e_i$  budget along the wall-normal direction in (a) M8T1 and (b) M8T2. All terms are normalized by  $\rho_w u_\tau^3 / \delta_\nu$ .

transfer exists far from the wall. Furthermore, the positive value of  $\overline{u_k'' \frac{\partial \sigma_{kj}}{\partial x_j}}$  represents the energy transfer from the mean flow to the fluctuating field and vice versa. It is depicted in Fig. 25 that  $\overline{u_k'' \frac{\partial \sigma_{kj}}{\partial x_j}}$  is dominated by its solenoidal component  $\overline{u_{s,k}'' \frac{\partial \sigma_{kj}}{\partial x_j}}$ .  $\overline{u_k'' \frac{\partial \sigma_{kj}}{\partial x_j}}$  mainly transfers energy from the mean flow to the fluctuating field in M8T2; however, in M8T1,  $\overline{u_k'' \frac{\partial \sigma_{kj}}{\partial x_j}}$  mainly transfers energy from the fluctuating field to the mean flow in the buffer layer, and reverse transfer exists far from the wall. Accordingly, both pressure work ( $\overline{u_k'' \frac{\partial p}{\partial x_k}}$ ) and viscous action ( $\overline{u_k'' \frac{\partial \sigma_{kj}}{\partial x_j}}$ ) can lead to a two-way exchange between mean flow and fluctuating field of kinetic energy.

It is found that all three interactions between mean-turbulent kinetic energy  $-\overline{\rho u_i'' u_j'' \frac{\partial \tilde{U}_i}{\partial x_j}}$ ,  $\overline{u_k'' \frac{\partial p}{\partial x_k}}$  and  $\overline{u_k'' \frac{\partial \sigma_{kj}}{\partial x_j}}$  are smaller in M8T1, indicating weaker energy transfer between mean and fluctuating kinetic energy with cold wall. Furthermore, the peak of the production term  $-\overline{\rho u_i'' u_j'' \frac{\partial \tilde{U}_i}{\partial x_j}}$  shifts farther away from the wall with the cold wall.

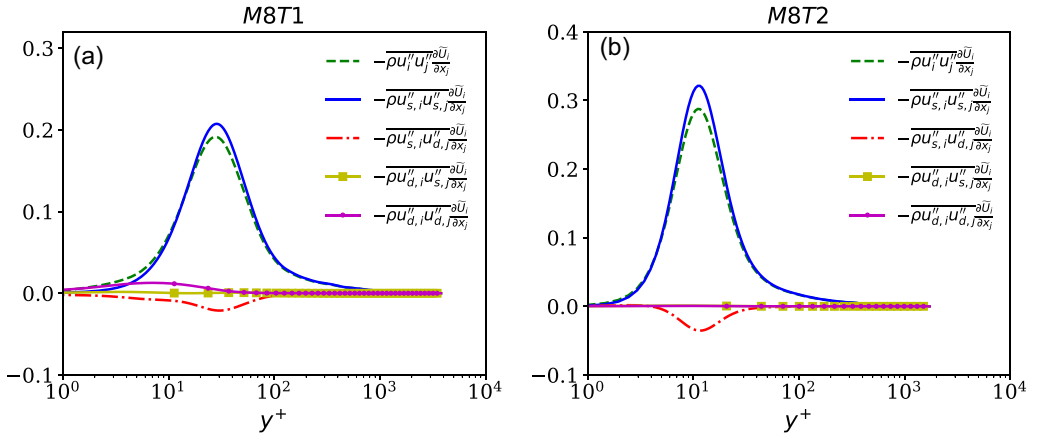


FIG. 23. The term  $-\overline{\rho u_i'' u_j'' \frac{\partial \tilde{U}_i}{\partial x_j}}$  and its decomposed components along the wall-normal direction in (a) M8T1 and (b) M8T2. All terms are normalized by  $\rho_w u_\tau^3 / \delta_\nu$ .

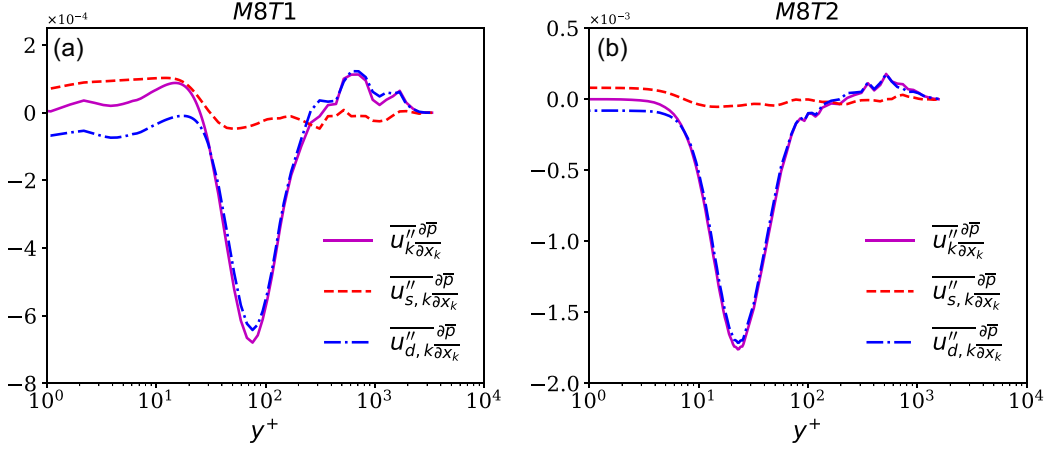


FIG. 24. The term  $\overline{u_k'' \frac{\partial \bar{p}}{\partial x_k}}$  and its decomposed components along the wall-normal direction in (a) M8T1 and (b) M8T2. All terms are normalized by  $\rho_w u_\tau^3 / \delta_v$ .

Next, the interactions between  $K_m$  and  $e_m$  are discussed. The most important interaction between  $K_m$  and  $e_m$  is through viscous action ( $\overline{\sigma_{ij} \frac{\partial \bar{U}_i}{\partial x_j}}$ ). Viscous action ( $\overline{\sigma_{ij} \frac{\partial \bar{U}_i}{\partial x_j}}$ ) dissipates mean field kinetic energy to mean field internal energy and is also dominated in the mean fields of kinetic and internal energy budgets. Another interaction is through the linear component of mean field pressure dilatation ( $\overline{\bar{p}_m \frac{\partial \bar{U}_k}{\partial x_k}}$ ). This term is two orders smaller than  $\overline{\sigma_{ij} \frac{\partial \bar{U}_i}{\partial x_j}}$  and has negligible contribution to the interactions between  $K_m$  and  $e_m$ . However, this term causes a two-way exchange. It is noted that the interactions between  $K_m$  and  $e_m$ ,  $\overline{\sigma_{ij} \frac{\partial \bar{U}_i}{\partial x_j}}$  and  $\overline{\bar{p}_m \frac{\partial \bar{U}_k}{\partial x_k}}$ , are similar in M8T1 and M8T2, indicating that the cold wall has negligible influence on the energy transfer between  $K_m$  and  $e_m$ .

The interaction between  $K_m$  and  $e_t$  is via the nonlinear component of mean field pressure dilatation ( $\overline{\bar{p}_r \frac{\partial \bar{U}_k}{\partial x_k}}$ ). This term is negligibly small and a two-way exchange.

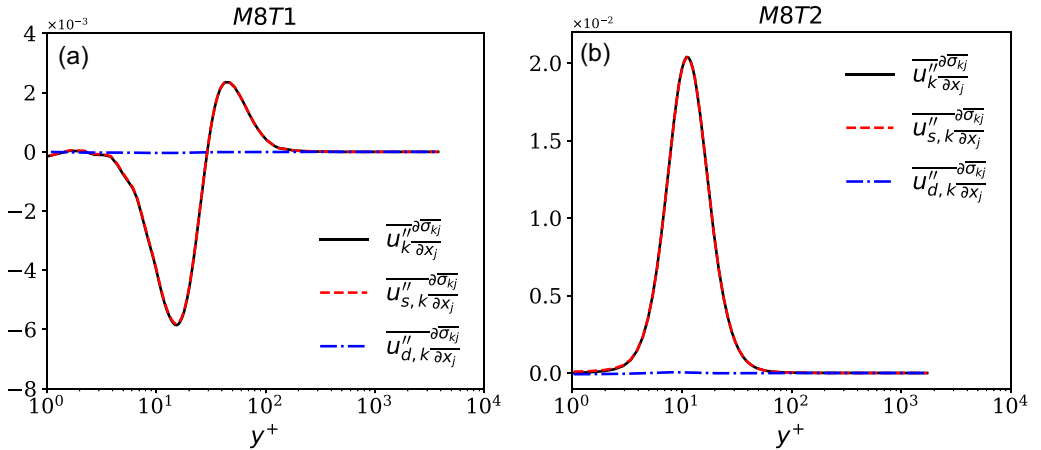


FIG. 25. The term  $\overline{u_k'' \frac{\partial \bar{\sigma}_{kj}}{\partial x_j}}$  and its decomposed components along the wall-normal direction in (a) M8T1 and (b) M8T2. All terms are normalized by  $\rho_w u_\tau^3 / \delta_v$ .

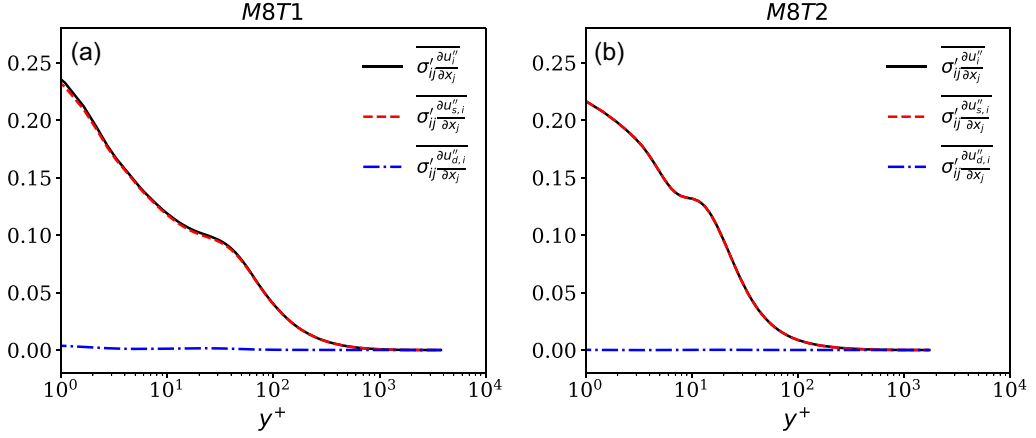


FIG. 26. The term  $\overline{\sigma'_{ij} \frac{\partial u''_i}{\partial x_j}}$  and its decomposed components along the wall-normal direction in (a) M8T1 and (b) M8T2. All terms are normalized by  $\rho_w u_\tau^3 / \delta_\nu$ .

The interaction between  $k$  and  $e_m$  is through fluctuating field viscous action ( $\overline{\sigma'_{ij} \frac{\partial u''_i}{\partial x_j}}$ ). The term  $\overline{\sigma'_{ij} \frac{\partial u''_i}{\partial x_j}}$  and its decomposed components along wall-normal direction in M8T1 and M8T2 are shown in Fig. 26. It is shown that the fluctuating field of kinetic energy dissipates energy into the mean field of internal energy via fluctuating field viscous action ( $\overline{\sigma'_{ij} \frac{\partial u''_i}{\partial x_j}}$ ). This term is dominated by its solenoidal components  $\overline{\sigma'_{ij} \frac{\partial u''_{s,i}}{\partial x_j}}$ . The dilatational component  $\overline{\sigma'_{ij} \frac{\partial u''_{d,i}}{\partial x_j}}$  has only a very weak contribution in the near-wall region. It is also found in Fig. 20 that  $\overline{\sigma'_{ij} \frac{\partial u''_i}{\partial x_j}}$  is dominated in the fluctuating field of kinetic energy budget, but is relative smaller compared with  $\overline{\sigma_{ij} \frac{\partial \bar{u}_i}{\partial x_j}}$  in the mean field of the internal energy budget (shown in Fig. 21), indicating that the mean field of kinetic energy contributes much more energy to the mean field of internal energy compared with the fluctuating field of kinetic energy. The cold wall has a pretty small influence on the energy transfer between  $k$  and  $e_m$ .

The interaction between  $k$  and  $e_t$  is through the fluctuating field pressure-dilatational action ( $\overline{p' \frac{\partial u'_k}{\partial x_k}}$ ). This term transfers energy from the fluctuating field of kinetic energy to the fluctuating field of internal energy entirely by its dilatational component.  $\overline{p' \frac{\partial u'_k}{\partial x_k}}$  is dominated in the fluctuating field of the internal energy budget and achieves its peak in the near-wall region. It is also shown that  $\overline{p' \frac{\partial u'_k}{\partial x_k}}$  is very small compared with the production term  $-\overline{\rho u''_i u''_j \frac{\partial \bar{u}_i}{\partial x_j}}$ . Furthermore,  $\overline{p' \frac{\partial u'_k}{\partial x_k}}$  in M8T1 is much larger than that in M8T2 near the wall, indicating that the cold wall enhances the compressibility near the wall and strengthens the energy transfer between  $k$  and  $e_t$ .

Finally, the interactions between  $e_m$  and  $e_t$  are discussed. The most important interaction is via viscous and thermal flux action ( $\overline{\frac{f\phi'}{\phi}}$ ).  $\overline{\frac{f\phi'}{\phi}}$  mainly transfers energy from the fluctuating field of internal energy to the mean field of internal energy and is dominated in fluctuating and mean fields of internal energy budgets. Another important interaction is through the linear component of the pressure-dilatational mechanism ( $\frac{2-\gamma}{2(\gamma-1)} \overline{p'_m \frac{\partial u'_k}{\partial x_k}}$ ). This term transfers energy from the mean field of internal energy to the fluctuating field of internal energy and is important in the fluctuating field of the internal energy budget. The last interaction is  $2u''_k \phi' \frac{\partial \phi}{\partial x_k}$ , which is shown in Fig. 27. This term is two orders smaller than above two interactions and is mainly governed by its solenoidal component

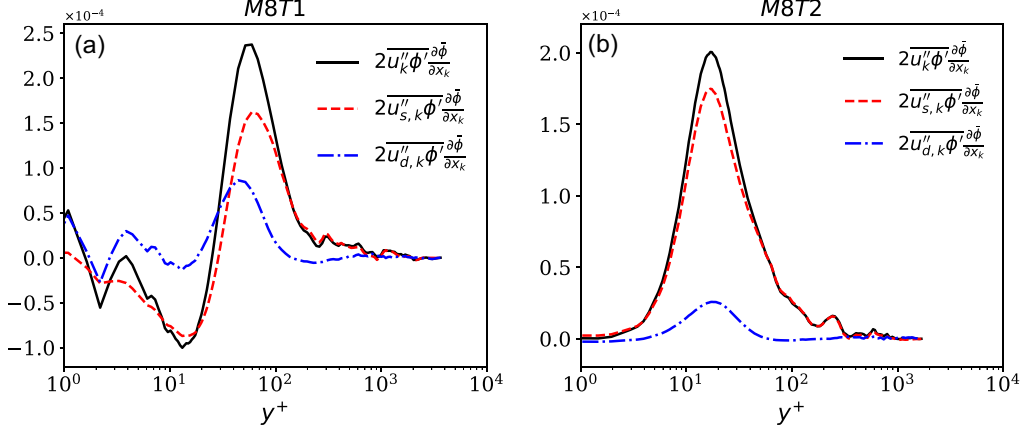


FIG. 27. The term  $2\overline{u''_k \phi'} \frac{\partial \bar{\phi}}{\partial x_k}$  and its decomposed components along the wall-normal direction in (a) M8T1 and (b) M8T2. All terms are normalized by  $\rho_w u_\tau^3 / \delta_v$ .

$2\overline{u''_{s,k} \phi'} \frac{\partial \bar{\phi}}{\partial x_k}$ . In M8T1,  $2\overline{u''_k \phi'} \frac{\partial \bar{\phi}}{\partial x_k}$  is a two-way exchange, and its dilatational component  $2\overline{u''_{d,k} \phi'} \frac{\partial \bar{\phi}}{\partial x_k}$  plays an important role due to large compressibility. It is shown that the cold wall has weak influence on the peak intensities of  $\frac{\bar{f} \phi'}{\phi}$  and  $2\overline{u''_k \phi'} \frac{\partial \bar{\phi}}{\partial x_k}$ , although a two-way exchange of  $2\overline{u''_k \phi'} \frac{\partial \bar{\phi}}{\partial x_k}$  appears with cold wall. However,  $\frac{2-\gamma}{2(\gamma-1)} p'_m \frac{\partial u''_k}{\partial x_k}$  is enhanced by the cold wall due to stronger compressibility.

Accordingly, it is concluded that most of the interactions are governed by the solenoidal components except for the terms associated with the pressure ( $\overline{u''_k \frac{\partial \bar{p}}{\partial x_k}}$  and  $\overline{p' \frac{\partial u''_k}{\partial x_k}}$ ), which are governed by the dilatational components. Moreover, the interactions between mean and fluctuating kinetic energy,  $-\overline{\rho u''_i u''_j \frac{\partial \bar{U}_i}{\partial x_j}}$ ,  $\overline{u''_k \frac{\partial \bar{p}}{\partial x_k}}$  and  $\overline{u''_k \frac{\partial \bar{\sigma}_{kk}}{\partial x_k}}$ , are weaker, while the interactions associated with dilatation ( $\overline{p' \frac{\partial u''_k}{\partial x_k}}$  and  $\frac{2-\gamma}{2(\gamma-1)} p'_m \frac{\partial u''_k}{\partial x_k}$ ) are enhanced due to higher values of  $\langle (\theta''^+)^2 \rangle^{1/2}$  in M8T1 [shown in Fig. 2(b)], and accordingly stronger compressibility near the wall with cold wall. Other interactions have small correlation with wall temperature.

## VII. SUMMARY AND CONCLUSION

In this paper, Helmholtz decomposition is introduced to investigate the compressibility effect of the isothermal hypersonic boundary layer. Two isothermal wall conditions with the freestream Mach number  $M_\infty = 8$  are studied, including the cold wall case  $T_w/T_\infty = 1.9$  and the less cold wall case  $T_w/T_\infty = 10.03$  denoted by M8T1 and M8T2, respectively. The PDF of normalized dilatation fluctuation  $\theta''^+$  in M8T1 is negatively skewed in the near-wall region, indicating that the cold wall condition enhances the compression motion near the wall. The Reynolds stress and decomposed components are investigated. It is noticed that  $R_{u_d u_d}^+$ ,  $R_{v_d v_d}^+$ , and  $R_{w_d w_d}^+$  are much larger in M8T1 than those in M8T2, indicating that the cold wall temperature can enhance the compressibility in the near-wall region. The instantaneous velocity fields demonstrate that  $u''$  exhibits the streaks, while  $v''$  has a more spotty appearance due to ejection and sweep events. The  $u''_d$  and  $v''_d$  behave as streamwise wave packets traveling from left to right.

Then the tensor  $M_{uv}^+$  and the turbulent shear stress  $R_{uv}^+$  are investigated meticulously. Quadrant analysis is introduced to explore the contributions of four events to the turbulent shear stress  $R_{uv}$ . It is found that the cold wall condition can enhance all four events in the near-wall region, and the increase of the Q2 (ejection) and Q3 (inward) events is larger than the Q1 (outward) and Q4 (sweep) events. The Q1 (outward) and Q2 (ejection) events are mainly located in the expansion region, while the Q3 (inward) and Q4 (sweep) events are primarily situated in the compression region near the

wall. Furthermore, it is found that the cold wall condition can enhance the Q3 (inward) event mainly in the compression region and the Q2 (ejection) event mainly in the expansion region near the wall. On the basis of Helmholtz decomposition, the properties of four decomposed components of the tensor  $M_{uv}^+$  are also discussed. It is found that the cold wall condition can enhance the positive  $u_s''$  and negative  $v_d''$  events, but has negligible influence on the  $u_d''$  and  $v_s''$ . Among four decomposed components,  $\langle M_{u_s v_s}^+ | \theta''^+ \rangle$  and  $\langle M_{u_s v_d}^+ | \theta''^+ \rangle$  are the dominant contributions to  $\langle M_{uv}^+ | \theta''^+ \rangle$ .  $\langle M_{u_s v_s}^+ | \theta''^+ \rangle$  is nearly independent on the wall temperature and gives the main contribution to  $\langle M_{uv}^+ | \theta''^+ \rangle$  far from the wall. However,  $M_{u_s v_d}^+$  is drastically influenced by wall temperature and dominant in  $\langle M_{uv}^+ | \theta''^+ \rangle$  near the wall. Detailed exploration demonstrates that the negative values of  $\langle M_{uv}^+ | \theta''^+ \rangle$  in the weak compression region at  $y^+ > 50$  in M8T1 and  $10 < y^+ < 100$  in M8T2 are mainly contributed by the Q2 and Q4 events of the solenoidal component  $M_{u_s v_s}^+$ . Furthermore, the strong positive values of  $\langle M_{uv}^+ | \theta''^+ \rangle$  in the compression region at  $5 < y^+ < 30$  are mainly due to the Q3 event of  $M_{u_s v_d}^+$ , and the strong negative values of  $\langle M_{uv}^+ | \theta''^+ \rangle$  in the expansion region at  $10 < y^+ < 100$  are primarily caused by the Q2 and Q4 events of  $M_{u_s v_s}^+$  and the Q2 event of  $M_{u_s v_d}^+$  in M8T1.

Moreover, the correlations between streamwise, wall-normal velocity fluctuations  $u''$ ,  $v''$ , and fluctuating temperature  $T'$  are also investigated. It is found that the cold wall enhances the positive correlation of  $C_{u''T'}$ , and suppresses the negative correlation of  $C_{v''T'}$  near the wall. However, the cold wall slightly weakens the negative correlation of  $C_{u''T'}$  and the positive correlation of  $C_{v''T'}$ , respectively, far from the wall. The effects of the dilatational components of  $C_{u''T'}$  and  $C_{v''T'}$  are dominant in the near-wall region, and the solenoidal components govern the correlations far from the wall.

Finally, the mean and fluctuating fields of kinetic and internal energy budgets as well as the interactions among  $K_m$ ,  $k$ ,  $e_m$ , and  $e_t$  are investigated. It is found that most of the interactions are governed by the solenoidal components. Things are different for the terms associated with the pressure ( $\overline{u_k'' \frac{\partial \bar{p}}{\partial x_k}}$  and  $\overline{p' \frac{\partial u_k''}{\partial x_k}}$ ), which are governed by the dilatational components. Furthermore, the interactions between mean and fluctuating kinetic energy are weaker, while the interactions associated with dilatation ( $\overline{p' \frac{\partial u_k''}{\partial x_k}}$  and  $\frac{2-\gamma}{2(\gamma-1)} \overline{p_m' \frac{\partial u_k''}{\partial x_k}}$ ) are stronger with the cold wall. The wall temperature has small influence on other interactions.

In conclusion, the compressibility effect in the hypersonic boundary layer with an isothermal wall condition is revealed with the introduction of Helmholtz decomposition. However, the compressibility effect on the flow structures, such as coherent structures, is not included in this paper, which is left for future studies.

## ACKNOWLEDGMENTS

This work was supported by the NSFC Basic Science Center Program (Grant No. 11988102), by the National Natural Science Foundation of China (NSFC Grants No. 91952104, No. 92052301 and No. 91752201), by the Technology and Innovation Commission of Shenzhen Municipality (Grants No. KQTD20180411143441009 and No. JCYJ20170412151759222), and by the Department of Science and Technology of Guangdong Province (Grant No. 2019B21203001). This work was also supported by the Center for Computational Science and Engineering of Southern University of Science and Technology.

## APPENDIX: VALIDATION OF THE ACCURACY OF THE CURRENT NUMERICAL SIMULATIONS

It is noted that the current numerical simulations have the same parameters as the database given in Refs. [22,23], and this database has been validated in previous investigations [22,23,31]. However, the current numerical simulations have a larger wall-normal and spanwise grid resolutions  $N_y$  and  $N_z$ , as well as a larger spanwise computational domain  $L_z$ . Therefore, the accuracy of the

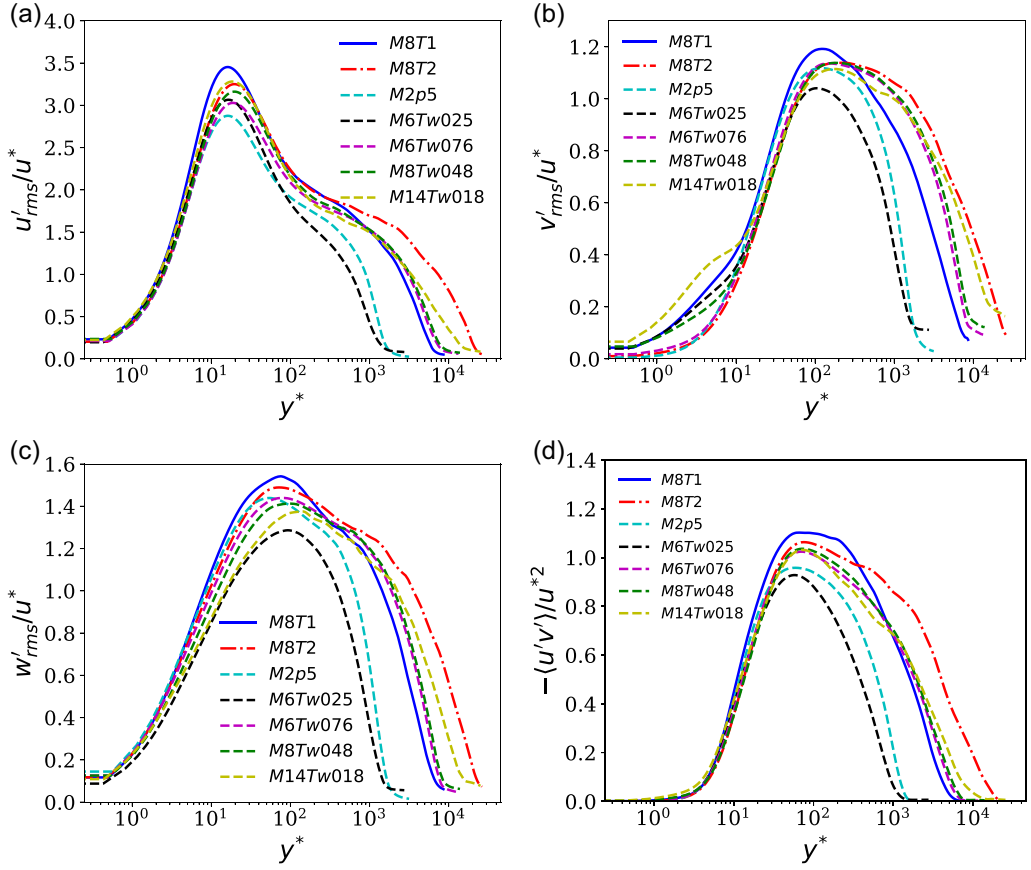


FIG. 28. Comparison of the normalized turbulent intensities and the normalized Reynolds shear stress between the current numerical simulations and the numerical simulations in Ref. [6]. (a) The normalized streamwise turbulent intensity; (b) the normalized wall-normal turbulent intensity; (c) the normalized spanwise turbulent intensity; (d) the normalized Reynolds shear stress. The labels M2p5, M6Tw025, M6Tw076, M8Tw048, and M14Tw018 represent the numerical simulations in Ref. [6].

current numerical simulations is further confirmed by comparing with the basic statistics of the numerical simulations in Ref. [6]. The wall-normal profiles of the normalized turbulent intensities and the normalized Reynolds shear stress are shown in Fig. 28. The turbulent intensities and Reynolds shear stress are normalized by  $u^*$ , which is expressed as  $u^* = \sqrt{\tau_w/\bar{\rho}} = u_\tau \sqrt{\bar{\rho}_w/\bar{\rho}}$ .  $y^*$  is defined as  $y^* = y/\delta_\tau^*$ , where  $\delta_\tau^* = \bar{\mu}/(\bar{\rho}u^*)$  is the semilocal scaling suggested in Ref. [55]. It is shown in Fig. 28 that the normalized turbulent intensities and normalized Reynolds shear stress of the current numerical simulations demonstrate good collapse with those in Ref. [6], which confirms the accuracy of the current numerical simulations.

- [1] A. J. Smits and J. P. Dussauge, *Turbulent Shear Layers in Supersonic Flow* (Springer-Verlag, New York, 2006).
- [2] T. Cebeci and A. M. O. Smith, *Analysis of Turbulent Boundary Layers* (Academic Press, New York, 1974).
- [3] T. B. Gatski and J. P. Bonnet, *Compressibility, Turbulence and High Speed Flow* (Elsevier, Amsterdam, 2009).

- [4] L. Duan, I. Beekman, and M. P. Martin, Direct numerical simulation of hypersonic turbulent boundary layers. Part 2. Effect of wall temperature, *J. Fluid Mech.* **655**, 419 (2010).
- [5] L. Duan, I. Beekman, and M. P. Martin, Direct numerical simulation of hypersonic turbulent boundary layers. Part 3. Effect of Mach number, *J. Fluid Mech.* **672**, 245 (2011).
- [6] C. Zhang, L. Duan, and M. Choudhari, Direct numerical simulation database for supersonic and hypersonic turbulent boundary layers, *AIAA J.* **56**, 4297 (2018).
- [7] M. P. Martin, Direct numerical simulation of hypersonic turbulent boundary layers. Part 1. Initialization and comparison with experiments, *J. Fluid Mech.* **570**, 347 (2007).
- [8] A. Marco, R. Camussi, M. Bernardini, and S. Pirozzoli, Wall pressure coherence in supersonic turbulent boundary layers, *J. Fluid Mech.* **732**, 445 (2013).
- [9] M. Ringuette, M. Wu, and M. P. Martin, Coherent structures in direct numerical simulation of turbulent boundary layers at Mach 3, *J. Fluid Mech.* **594**, 59 (2008).
- [10] F. Alizard, S. Pirozzoli, M. Bernardini, and F. Grasso, Optimal transient growth in compressible turbulent boundary layers, *J. Fluid Mech.* **770**, 124 (2015).
- [11] P. Bradshaw, Compressible turbulent shear layers, *Annu. Rev. Fluid Mech.* **9**, 33 (1977).
- [12] Q. Li and G. N. Coleman, DNS of an oblique shock wave impinging upon a turbulent boundary layer, *Direct and Large-Eddy Simulation V* (Springer, Dordrecht, 2004), pp. 387–396.
- [13] S. E. Guarini, R. D. Moser, K. Shariff, and A. Wray, Direct numerical simulation of a supersonic turbulent boundary layer at Mach 2.5, *J. Fluid Mech.* **414**, 1 (2000).
- [14] M. Lagha, J. Kim, J. D. Eldredge, and X. Zhong, A numerical study of compressible turbulent boundary layers, *Phys. Fluids* **23**, 015106 (2011).
- [15] S. Pirozzoli, F. Grasso, and T. B. Gatski, Direct numerical simulation and analysis of a spatially evolving supersonic turbulent boundary layer at  $M = 2.25$ , *Phys. Fluids* **16**, 530 (2004).
- [16] S. Pirozzoli, M. Bernardini, and F. Grasso, On the dynamical relevance of coherent vortical structures in turbulent boundary layers, *J. Fluid Mech.* **648**, 325 (2010).
- [17] S. Pirozzoli and M. Bernardini, Turbulence in supersonic boundary layers at moderate Reynolds number, *J. Fluid Mech.* **688**, 120 (2011).
- [18] S. Pirozzoli, M. Bernardini, and F. Grasso, Characterization of coherent vortical structures in a supersonic turbulent boundary layer, *J. Fluid Mech.* **613**, 205 (2008).
- [19] S. Pirozzoli, On the size of the energy-containing eddies in the outer turbulent wall layer, *J. Fluid Mech.* **702**, 521 (2012).
- [20] T. Maeder, N. A. Adams, and L. Kleiser, Direct simulation of turbulent supersonic boundary layers by an extended temporal approach, *J. Fluid Mech.* **429**, 187 (2001).
- [21] T. Maeder, Numerical investigation of supersonic turbulent boundary layers, Ph.D. thesis, ETH, Zurich, 2000.
- [22] X. Liang and X. Li, DNS of a spatially evolving hypersonic turbulent boundary layer at Mach 8, *Sci. China Phys. Mech. Astron.* **56**, 1408 (2013).
- [23] X. Liang and X. Li, Direct numerical simulation on Mach number and wall temperature effects in the turbulent flows of flat-plate boundary layer, *Commun. Comput. Phys.* **17**, 189 (2015).
- [24] Y. Chu, Y. Zhuang, and X. Lu, Effect of wall temperature on hypersonic turbulent boundary layer, *J. Turbul.* **14**, 37 (2013).
- [25] L. Wang and X. Lu, Flow topology in compressible turbulent boundary layer, *J. Fluid Mech.* **703**, 255 (2012).
- [26] Y. S. Zhang, W. T. Bi, F. Hussain, X. L. Li, and Z. S. She, Mach-Number-Invariant Mean-Velocity Profile of Compressible Turbulent Boundary Layers, *Phys. Rev. Lett.* **109**, 054502 (2012).
- [27] Y. Zhang, W. Bi, F. Hussain, and Z. She, A generalized Reynolds analogy for compressible wall-bounded turbulent flows, *J. Fluid Mech.* **739**, 392 (2014).
- [28] Z. She, H. Zou, M. Xiao, X. Chen, and F. Hussain, Prediction of compressible turbulent boundary layer via a symmetry-based length model, *J. Fluid Mech.* **857**, 449 (2018).
- [29] B. Wu, W. Bi, F. Hussain, and Z. She, On the invariant mean velocity profile for compressible turbulent boundary layers, *J. Turbul.* **18**, 186 (2017).



- [30] Y. Chu and X. Lu, Topological evolution in compressible turbulent boundary layers, *J. Fluid Mech.* **733**, 414 (2013).
- [31] X. Li, F. Tong, C. Yu, and X. Li, Statistical analysis of temperature distribution on vortex surfaces in hypersonic turbulent boundary layer, *Phys. Fluids* **31**, 106101 (2019).
- [32] J. Wang, M. Wan, S. Chen, and S. Chen, Kinetic energy transfer in compressible isotropic turbulence, *J. Fluid Mech.* **841**, 581 (2018).
- [33] J. Wang, Y. Shi, L. Wang, Z. Xiao, X. He, and S. Chen, Effect of compressibility on the small-scale structures in isotropic turbulence, *J. Fluid Mech.* **713**, 588 (2012).
- [34] J. Wang, Y. Shi, L. P. Wang, Z. Xiao, X. T. He, and S. Chen, Scaling and Statistics in Three-Dimensional Compressible Turbulence, *Phys. Rev. Lett.* **108**, 214505 (2012).
- [35] J. Wang, T. Gotoh, and T. Watanabe, Shocklet statistics in compressible isotropic turbulence, *Phys. Rev. Fluids* **2**, 023401 (2017).
- [36] J. Wang, T. Gotoh, and T. Watanabe, Scaling and intermittency in compressible isotropic turbulence, *Phys. Rev. Fluids* **2**, 053401 (2017).
- [37] J. Wang, Y. Yang, Y. Shi, Z. Xiao, X. T. He, and S. Chen, Cascade of Kinetic Energy in Three-Dimensional Compressible Turbulence, *Phys. Rev. Lett.* **110**, 214505 (2013).
- [38] J. Wang, M. Wan, S. Chen, C. Xie, Q. Zheng, L. Wang, and S. Chen, Effect of flow topology on the kinetic energy flux in compressible isotropic turbulence, *J. Fluid Mech.* **883**, A11 (2020).
- [39] Q. Zheng, J. Wang, B. R. Noack, H. Li, M. Wan, and S. Chen, Vibrational relaxation in compressible isotropic turbulence with thermal non-equilibrium, *Phys. Rev. Fluids* **5**, 044602 (2020).
- [40] J. Teng, J. Wang, H. Li, and S. Chen, Spectra and scaling in chemically reacting compressible isotropic turbulence, *Phys. Rev. Fluids* **5**, 084601 (2020).
- [41] S. Chen, J. Wang, H. Li, M. Wan, and S. Chen, Spectra and Mach number scaling in compressible homogeneous shear turbulence, *Phys. Fluids* **30**, 065109 (2018).
- [42] S. Chen, J. Wang, H. Li, M. Wan, and S. Chen, Effect of compressibility on small scale statistics in homogeneous shear turbulence, *Phys. Fluids* **31**, 025107 (2019).
- [43] S. Chen, X. Wang, J. Wang, H. Li, M. Wan, and S. Chen, Effects of bulk viscosity on compressible homogeneous turbulence, *Phys. Fluids* **31**, 085115 (2019).
- [44] X. Wang, S. Chen, J. Wang, H. Li, M. Wan, and S. Chen, Effect of compressibility on the local flow topology in homogeneous shear turbulence, *Phys. Fluids* **32**, 015118 (2020).
- [45] M. Yu, C. X. Xu, and S. Pirozzoli, Genuine compressibility effects in wall-bounded turbulence, *Phys. Rev. Fluids* **4**, 123402 (2019).
- [46] D. S. Balsara and C. Shu, Monotonicity preserving weighted essentially non-oscillatory schemes with increasingly high order of accuracy, *J. Comput. Phys.* **160**, 405 (2000).
- [47] X. Li, D. Fu, and Y. Ma, Direct numerical simulation of hypersonic boundary layer transition over a blunt cone, *AIAA J.* **46**, 2899 (2008).
- [48] H. Gao, D. Fu, Y. Ma, and X. Li, Direct numerical simulation of supersonic turbulent boundary layer flow, *Chin. Phys. Lett.* **22**, 1709 (2005).
- [49] M. M. Rai, T. B. Gatski, and G. Erlebacher, Direct simulation of spatially evolving compressible turbulent boundary layers, in *Proceedings of the 33rd Aerospace Sciences Meeting and Exhibit, 1995* (AIAA, Reston, VA, 1995), p. 583.
- [50] G. Hirasaki and J. Hellums, Boundary conditions on the vector and scalar potentials in viscous three-dimensional hydrodynamics, *Q. App. Math.* **28**, 293 (1970).
- [51] E. R. Van Driest, Turbulent boundary layer in compressible fluids, *J. Aeronaut. Sci.* **18**, 145 (1951).
- [52] A. A. Townsend, *The Structure of Turbulent Shear Flow* (Cambridge University Press, Cambridge, 1976).
- [53] J. M. Wallace, Quadrant analysis in turbulence research: History and evolution, *Annu. Rev. Fluid Mech.* **48**, 131 (2016).
- [54] A. Mittal and S. S. Girimaji, Mathematical framework for analysis of internal energy dynamics and spectral distribution in compressible turbulent flows, *Phys. Rev. Fluids* **4**, 042601(R) (2019).
- [55] P. G. Huang, G. Coleman, and P. Bradshaw, Compressible turbulent channel flows: DNS results and modelling, *J. Fluid Mech.* **305**, 185 (1995).